Initial Time Dependence of Wind- and Density-driven Lagrangian Residual Velocity in a Tide-dominated Bay

Guangliang Liu[1], Zhe Liu[2], Huiwang Gao[2], and Shizuo Feng[2]

[1]Shandong Provincial Key Laboratory of Computer Networks Shandong Computer Science Center (National Supercomputer Center in Jinan)
[2]Ocean University of China

November 24, 2022

Abstract

The nonlinear effect of the summer SE wind and density on the 3D structures of the full Lagrangian residual velocity (LRV) was quantified for a general nonlinear system, using Jiaozhou Bay, China (JZB), as the test site. In the tidally energetic JZB, the basic patterns of the wind- and density-driven full LRV were found to be consistent with simplified semi-analytical solutions but highly dependent on the initial times. The wind-driven full LRVs detected at different tidal phases showed similar laterally sheared, three-layer circulation, but the main branches could migrate across nearly half of the inner bay. The density-driven, clockwise flow dominated the western inner bay at low tide, while almost disappearing at high tide. The effect of density generally enhanced outward flow in the surface layer and inward flow in the bottom layer. Along-trajectory, integrated momentum balances indicated that viscosity was the main force responsible for the time-dependence of the wind-driven full LRV, while viscosity and the barotropic and baroclinic pressure gradients were the main drivers of the intra-tidal variations in the density-driven full LRV. Generally, the summer wind and density had opposing effects, although their influence was weaker than that of the tide and could not change the patterns of the tide-driven full LRV. The results indicated that when the effects of wind and density on the coastal circulation of tidally energetic waters are analysed, both the 3D structures and the possibility of a high initial tidal phase dependency should be considered.

Initial Time Dependence of Wind- and Density-driven Lagrangian Residual Velocity in a Tide-dominated Bay

Guangliang Liu[1, 2], Zhe Liu[2*, ++], Huiwang Gao[2] and Shizuo Feng[2]

[1]Shandong Computer Science Center (National Supercomputer Center in Jinan), Shandong Provincial Key Laboratory of Computer Networks, Qilu University of Technology (Shandong Academy of Sciences), Jinan 250101, China

[2] Key Laboratory of Marine Environment and Ecology, Ministry of Education, Ocean University of China, Qingdao 266100, China.

[++]Now works in the Department of Earth Sciences, National Natural Science Foundation of China.

Corresponding author: Zhe Liu (zliu@ouc.edu.cn)

Key Points:

- Wind and density influence on full Lagrangian residual velocity (LRV) was highly dependent on initial time in tidally energetic Jiaozhou Bay
- The basic patterns of wind- and density-driven full LRV were consistent with semi-analytical solutions
- The momentum balance, integrated along particle trajectories, explained intra-tidal variations in wind and density effects on the full LRV

Abstract

The nonlinear effect of the summer SE wind and density on the 3D structures of the full Lagrangian residual velocity (LRV) was quantified for a general nonlinear system, using Jiaozhou Bay, China (JZB), as the test site. In the tidally energetic JZB, the basic patterns of the wind- and density-driven full LRV were found to be consistent with simplified semi-analytical solutions but highly dependent on the initial times. The wind-driven full LRVs detected at different tidal phases showed similar laterally sheared, three-layer circulation, but the main branches could migrate across nearly half of the inner bay. The density-driven, clockwise flow dominated the western inner bay at low tide, while almost disappearing at high tide. The effect of density generally enhanced outward flow in the surface layer and inward flow in the bottom layer. Along-trajectory, integrated momentum balances indicated that viscosity was the main force responsible for the time-dependence of the wind-driven full LRV, while viscosity and the barotropic and baroclinic pressure gradients were the main drivers of the intra-tidal variations in the density-driven full LRV. Generally, the summer wind and density had opposing effects, although their influence was weaker than that of the tide and could not change the patterns of the tide-driven full LRV. The results indicated that when the effects of wind and density on the coastal circulation of tidally energetic waters are analysed, both the 3D structures and the possibility of a high initial tidal phase dependency should be considered.

Plain Language Summary

Recent research has shown that full Lagrangian residual velocity should be used to describe coastal circulations rather than Eulerian residual velocity. Compared to wind- and density-driven Eulerian residual velocity, the wind- and density-driven full Lagrangian residual velocities in tidally dominated coastal seas have seldom been discussed in previous studies. The work described here has shown that the effects of wind and density on tidally energetic waters exhibit not only 3D structures but also high levels of initial tidal phase dependency. In Jiaozhou Bay, we found that the main branches of the wind-driven Lagrangian residual current could move half of the inner bay, in different tidal phases, and that the density-driven, clockwise flow dominated the western inner bay at low tide, while almost disappearing at high tide.

1 Introduction

It is residual velocity rather than instantaneous oscillating tidal currents **that determines subtidal mass transport processes in coastal waters**, where tides often play a dominant role, leading to periodic velocities during a tidal cycle. There are two types of residual velocity—Eulerian residual velocity (ERV) and Lagrangian residual velocity (LRV). Full LRV is defined as the net replacement per tidal cycle (Zimmerman, 1979; Feng et al., 2008) and can be calculated as shown in Eq. (1):

$$\vec{u}_L(\vec{x}_0, t_0) = \frac{\vec{\xi}_{nT}}{nT} \tag{1}$$

where $\vec{u}_L(\vec{x}_0, t_0)$ represents the full LRV with the initial position vector ($\vec{x}_0$), and the initial intra-tidal process-independent time (t_0) for an arbitrary water parcel to be tracked; $\vec{\xi}_{nT}$ denotes the net displacement of an arbitrarily labelled water parcel over *n* tidal periods, *T*. The ERV can be obtained by means of a fixed current velocity meter, averaged over the tidal cycle:

$$\vec{u}_E = \langle \vec{u} \rangle \tag{2}$$

where <> indicates the tidal cycle mean function. The LRV has the inherent ability to include complete information on coastal subtidal circulation (Zimmerman, 1979; Cheng and Casulli, 1982), while the ERV represents the 0-order of the LRV (Feng et al., 1986a; Feng et al., 2008). **The discrepancy between LRV and ERV relies on the degree of nonlinearity in the applicable hydrodynamics.**

The hydrodynamics in coastal waterbodies—such as tidal estuaries and shallow bays—usually feature nonlinear effects that are relatively stronger than those of marginal seas or open oceans. The relative importance of nonlinear processes can be roughly measured as shown in Eq. (3):

$$\kappa = \eta_c / h_c \tag{3}$$

where κ is a dimensionless parameter, and η_c and h_c are characteristic values for water elevation (η) and undisturbed water depth (h), respectively (Feng et al., 1986a; Feng et al., 2008). From marginal seas / open oceans to coastal waters, water depth, h, decreases with topography, while water elevations (i.e., usually tidal elevation), η, increase due to wave shoaling effects—so that, as a result, κ increases, indicating stronger nonlinearity. In addition, irregular coastlines enhance the flow field gradient, which also results in stronger nonlinearity, so that **discrepancies between LRV and ERV become significant as a consequence.**

In most cases, coastal water bodies can be categorized by ‘weakly’ and ‘general’ nonlinear hydrodynamic systems. In a weakly nonlinear system, $\kappa \ll 1$, while for a general nonlinear system, κ is generally less than but sometimes can be comparable to 1.

Regarding weakly nonlinear hydrodynamics systems, the LRV can be simplified into its first order form, also called the mass transport velocity (MTV) (Feng et al., 1986a; Feng, 1990; Feng et al., 2008). The MTV, $\vec{u}_M$ can be calculated as shown in Eq. (4):

$$\vec{u}_M = \vec{u}_E + \vec{u}_S \tag{4}$$

where $\vec{u}_S$ denotes the Stokes drift (SD). In some occasions, the ERV can show a pattern quite similar to the MTV, owing to a small SD, which is why ERV is a widely used parameter in coastal oceanography (e.g., Delhez, 1996; Winant, 2004; Klingbeil et al., 2019). On some occasions, however, the SD cannot be negligible, resulting in an obvious discrepancy between the ERV and MTV (e.g., Feng et al., 1986a; Jiang and Feng, 2011, 2014). Analytical solutions in ideal domains (e.g., Ianniello, 1977; Winant, 2008; Jiang and Feng, 2011) show that MTVs satisfy the mass conservation law, while ERVs cannot. This finding has been confirmed in more and more laboratory experiments (e.g. Wang et al., 2013; Chen et al., 2017) and numerical modelling studies (e.g., Quan et al., 2014; Deng et al., 2017, 2019; Cui et al., 2018, 2019).

However, in a general nonlinear hydrodynamic system, the coastal circulation has to be described by full LRVs, rather than MTVs or ERVs. A full LRV can be expressed as the sum of the ERV ($\vec{u}_E$), SD ($\vec{u}_S$), Lagrangian drift velocity ($\vec{u}_{ld}$) and a higher order of extension (Feng et al., 1986a; Feng et al., 2008), as shown in Eq. (5):

$$\vec{u}_L = \vec{u}_E + \vec{u}_S + \kappa\vec{u}_{ld} + O(\kappa^2) \tag{5}$$

MTV cannot be used very well as a substitute for LRV, due to the vital importance of the absent high-order terms—such as Lagrangian drift velocity, $\vec{u}_{ld}$, (Feng et al., 1986a; Feng et al., 2008; Jiang and Feng, 2011). Therefore, full LRV must be used to describe a mass transport trend. The distinction between weakly and general hydrodynamic fields that **full LRV varies with initial tidal phase is significant, as ERV and MTV do not (e.g., Feng et al., 2008; Ju et al., 2009).** Liu et al. (2012) compared simulated M_2 tide-driven ERVs, MTVs, and full LRVs for Jiaozhou Bay (JZB), a general nonlinear hydrodynamic system, and further confirmed this theory. They found that only the full LRV could satisfactorily explain the net transport pattern of surface sediment. Xu et al. (2016) found that the full LRV presented a reasonable spatial pattern, which could explain intertidal salinity transport, while ERV could not (Xu et al., 2016).

The roles of wind and density on LRVs have not been clarified, especially for general nonlinear coastal systems. Although oscillating tidal currents are often the most energetic motion in shallow waters, their net influence can be one-orderly smaller, as the periodically oscillating components of tidal currents would naturally cancel themselves. In contrast with tidal currents, wind- and density-driven velocities are quasi-constant, within a tidal scale, and it should be pointed out that numerous studies have been conducted on the influence of wind and density on ERV and MTV (e.g., Wang et al., 1993; Muller et al., 2009; Muller et al., 2010; Geyer and MacCready, 2014; Lange and Burchard, 2019). **Compared to ERV and MTV, however, little is known about the influence of wind and density on a full LRV**, which determines subtidal transport in general nonlinear hydrodynamics systems.

The purpose of this study was to quantify the effects of wind and density on the three-dimensional (3D) structures of full LRV in a general nonlinear bay, JZB, China. The paper has been organized as follows: the study area, JZB, has been described in Section 2, while model setup and the measuring methods used to establish the effects of wind and density on the full LRV, and the Ekman ($\mathrm{E_k}$), Kelvin (K_e), and Wedderburn (W) numbers (three dimensionless parameters), have been presented in Section 3. Model validation has been described in Section 4, while the residual velocities in the tide-wind-density system, and wind and density effects on the full LRV, have been described in Section 5. Further insights into the structures of the full LRV have been gained by examining the three dimensionless parameters and semi-analytical solutions, in Section 6. Momentum balance analyses, integrated along particle trajectories, have been used to explain intra-tidal variation in wind- and density-driven full LRVs in Section 7, while the competition between wind and density effects on residual velocities has been described in Section 8. The main conclusions of this study have been summarized in the final section.

2 Study Area

The study area, JZB, is a semi-enclosed, tidally dominated, shallow bay, located in northern China (Figure 1), that is connected to the Yellow Sea through a narrow mouth (~ 3 km). The mean depth is approximately 7 m, with the maximum being > 60 m, at the bay mouth. It has an area of ~ 354 km^2, with up to one third occupied by tidal flats. The predominant seawater movement is a semidiurnal (M_2) tide, which provides over 80 % of the kinetic and potential energy in the seawater (Ding, 1992). The tidal current is characterized as a rectilinear current, and its amplitude can reach 1.2 m.

JZB can be divided into two parts, known as Inner Bay and Outer Bay, by a line between Tuandao and Huangdao. In the shallow Inner Bay, the mean κ is ~ 0.2 in the northern shallow region, while the wide tidal flat provides a notable increase in the nonlinearity of the hydrodynamics. In the deep Outer Bay, the hydrodynamics are highly nonlinear, due to the irregular coastline and complex topography. Thus, JZB can be designated as a general nonlinear system, rather than a weakly nonlinear system.

It has been reported that wind and density are important to JZB hydrodynamics in summer (Wang and Gao, 2003; Cai et al., 2014). Long-term meteorological and hydrographic records are available for the bay, extending back to the 1930s, while hydrodynamic observations have been accumulated more recently (Zhang, 2007). The annual average JZB wind speed is approximately 5.4 m·s^{-1}; the SE wind prevails in summer, with a speed of 5.0 m·s^{-1}, while the NW wind prevails in winter, with a speed of 6.3 m·s^{-1} (Editorial Board of Annals in China, 1993; Wang and Gao, 2003). Over 80% of the freshwater input to the bay comes from seasonal flows in the Dagu River (Chen et al., 2007), with 87.10% of its annual discharge (approximately 3.02 × 10^{8} m^{3}·y^{-1}) occurring in the summer (Jiang and Wang, 2013). Under this river's influence, intra-tidal variation of seawater salinity and density can reach 1.50 and 1.5 kg·m^{-3}, respectively, around the Dagu River mouth, and a little less than 0.50 and 0.5 kg·m^{-3} in the vicinity of the bay mouth (Cai et al., 2014).

Previous studies have characterised the residual velocities of the JZB marine environment. Using a barotropic tidal current model in this previous work, the authors calculated the tide-driven ERV, MTV, and full LRV, in JZB, and found that the full LRV showed large intra-tidal variations and was the only type of residual velocity that could account for the net transport pattern for the surface sediments (Liu et al., 2012). Cai et al. (2014), using synchronous observational water temperature and salinity data, indicated that the summer, density-driven JZB currents had the same order as the ERV, while Lin et al. (2015) analysed the dynamics governing the response of the ERV along the JZB mouth to land reclamation. As mentioned in Section 1, the influence of wind and density on the full LRV general nonlinear system have not been discussed previously, so in this follow-up case study, the authors have qualified wind and density effects on the full LRV in JZB, a general nonlinear bay.

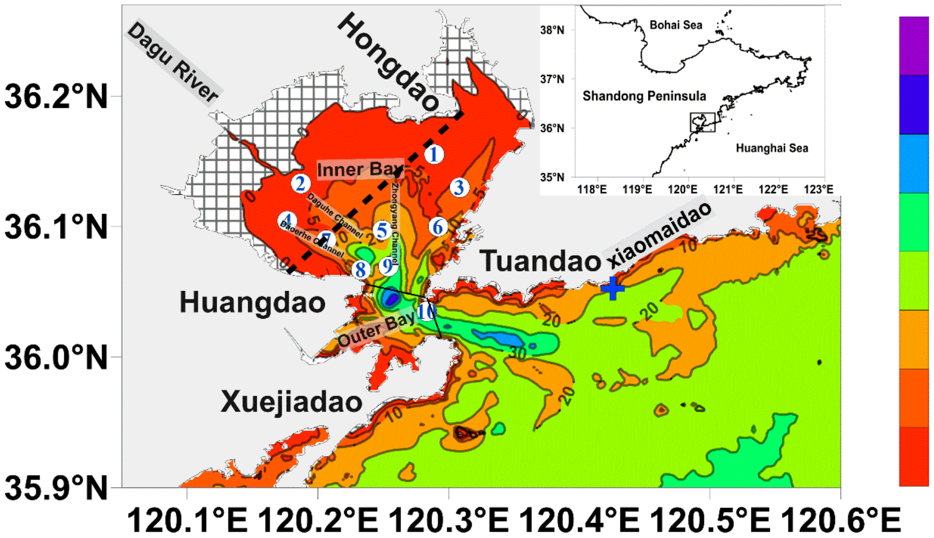

Figure 1. *JZB bathymetry (m). The gridded region represents tidal flats. JZB can be divided into the Inner Bay and Outer Bay by the solid line between Tuandao and Huangdao. The bay channel connecting JZB to the Yellow Sea is located between Tuandao and Xuejiadao. The blue cross represents the Xiaomaidao meteorological observation station. The numbered white circles denote the sampling stations where synchronous observations were conducted during*

August 2009. The dashed line between Huangdao and Hongdao indicates the section used both for momentum balance analyses and to compare the simulated and analytical solutions for wind- and density-driven residual velocities discussed in Section 6.

3 Methods

3.1 Model description

Since the M_2 tidal component is dominant, a hydrodynamic model with a particle tracking module—that is, the Princeton Ocean Model (POM)—which is driven by only the M_2 semidiurnal tidal component, has been established in JZB (Cai et al., 2014; Liu et al., 2012).

The POM has been used to simulate 3D hydrodynamics in JZB, and, as can be seen in Figure 1, the domain was divided into a 312 × 213 grid, with a horizontal grid element size of approximately 200 × 250 m, while 17 vertical sigma levels provided an average vertical resolution of approximately 0.5 m. The time steps for the external and internal modes were 0.8 and 4.0 s, respectively. The model domain included the tidal flats, using the Wetting and Drying technique, while vertical mixing was investigated using the Mellor–Yamada level 2.5 turbulence closure model (Mellor and Yamada 1982), whose horizontal mixing coefficients were calculated using a Smagorinsky-type formulation (Smagorinsky et al. 1965).

The initial temperature and salinity fields were diagnosed using the method of Cai et al. (2014). The hydrographic and meteorological datasets originated from synchronous observations taken at 21 anchor stations, in August 2009 (Liu et al., 2013; Cai et al., 2014). The SE wind predominates in summer, with a magnitude of approximately 5.0 $m \cdot s^{-1}$ (Editorial Board of Annals in China, 1993). Discharge from the Dagu River was estimated using a correlation model which linked river discharge to precipitation (Jiang and Wang, 2016). At the open boundaries, the tidal elevation was specified, with the tidal amplitudes, phases, potential temperature and salinity there obtained from the Marine Atlas of the Bohai Sea, Yellow Sea, East China Sea (Chen 1992).

Solar radiation was employed in the model, using a double exponential absorption function (Paulson and Simpson, 1977) with Jerlov water type II parameters. The net longwave heat flux into the ocean was estimated using bulk formulae evaluated by Fung et al. (1984), while wind stress, latent heat flux, and sensible heat flux were calculated from bulk formulae (Fairall et al., 1996), using the COARE3.0 parameterization scheme (Fairall et al., 2003). The model was run over 40 tidal cycles.

Labelled particles were tracked over one M_2 tidal period for different tidal phases, using the water parcel tracking module applied by Liu et al. (2012) to calculate the full LRV. Initially, water parcels were deployed in every sigma layer in each wet cell in Figure 1. Since the full LRV has been shown to be very dependent on initiating time, it will be referred to as the full LRV at the initial tidal phases in latter sections, and the tidal period was divided into 12 equal initial tidal phases from the initial release time. The 3D full LRV was calculated first, and the depth- or tide-averaged full LRV was developed after. Lagrangian residual transport velocity, $\vec{u}_{LT}$, was used to estimate the overall net transport, as shown in Eq. (6):

$$\vec{u}_{LT} = \frac{\langle (h+\eta_L)\vec{\bar{u}}_L \rangle}{\langle h+\eta_L \rangle} \tag{6}$$

where $\vec{\bar{u}}_L$ represents the depth-averaged Lagrangian residual velocity; η_L denotes the Lagrangian intertidal free surface, equal to the free surface where an arbitrarily labelled water parcel locates over *n* tidal cycles (Feng et al., 2008). The overbar refers to a depth-averaged function.

3.2 Numerical experiments

To address the main dynamic progress, the predominant, M_2, semidiurnal tidal component, the prominent wind in summer, and the diagnosed distributions of potential temperature and salinity from Cai et al. (2014) were considered in the tide–wind–density system.

The numerical experiments used to investigate the effects of wind and density on residual velocity have been listed in Table 1. The tide-wind-density driven full LRV was calculated as the control run (Case 1), and the tide-density and tide-wind driven full LRVs were calculated as Case 2 and Case 3, respectively. In Case 2 and Case 3, the influencing dynamic factors, including wind and density, were separately removed. The difference was regarded as the effect of the influencing dynamic factor on the full LRV in the tide-wind-density system. Since the tide was the dominant seawater movement variable, all numerical experiments included tides, and if the wind- or density-driven full LRVs had the same direction as the full LRV in the tide-wind-density system, then this factor was deemed to have played a positive role in the full LRV, and vice versa.

Table 1. Numerical experiments used to investigate the effects of wind and density on residual velocity

Case	Dynamics Factors	Output	Description
1	Tide, Wind, Density	Complete processes	Control run
2	Tide, Density	Wind-driven residual velocity	Wind excluded from Case 1

3	Tide, Wind	Density-driven residual velocity	Density excluded from Case 1

3.3 Dimensionless parameters

To analyse the effects of wind and density qualitatively, the Ekman (E_k), Kelvin (K_e) and Wedderburn (W) numbers, which are three key parameters associated with the flow pattern and dynamics of wind- and density-driven flows, were calculated. These parameters have been widely used in coastal studies to examine the controlling dynamics of flow patterns (e.g., Valle-Levinson, 2008; Li and Li, 2011; Jia and Li, 2012).

The Ekman number, E_k, compares friction to Coriolis effects, as shown in Eq. (7):

$$E_k = A_z/(fh^2) \tag{7}$$

where A_z denotes flow eddy viscosity. At each horizontal grid point, we estimated A_z as the depth-averaged value of the eddy viscosity calculated from the model. The Coriolis parameter is represented by f.

The Kelvin number, K_e can be obtained as shown in (8):

$$K_e = B/R_i \tag{8}$$

where B refers to basin width (Garvine, 1995). R_i is given by $(g'h)^{1/2}/f$, where $g' = g\Delta\rho'/\rho_0$ denotes the reduced gravity, g represents gravitational acceleration, $\Delta\rho'$ indicates the contrast between buoyant water density and density in the bottom layer, while ρ_0 stands for a reference water density. Basin width determines whether the Earth's rotational effect on density-driven or wind-driven water exchange is appreciable (Pritchard, 1952; Valle-Levinson, 2008).

The relative importance of wind-driven and gravitational circulations can be measured using the Wedderburn number (Monismith, 1986) (Eq. (9)):

$$W = \frac{L\tau_{wx}}{\Delta\rho g {h_{mean}}^2} \tag{9}$$

where τ_{wx} denotes the along-channel wind, L represents basin length, $\Delta\rho$ stands for the density change over L, and h_{mean} shows the averaged depth. Wind-driven circulation is dominant when $W > 1$, while gravitational circulation is dominant when $W < 1$ (Geyer, 1997).

4. Model validation

4.1 Hydrodynamics field

The hydrodynamic model was calibrated with the observed tidal ellipse parameters for the M_2 currents at ten anchor stations, using observed temperature and salinity in the surface and bottom layers, at high and low tides (Figure 1).

Tidal ellipse parameters for a semidiurnal tide, recorded at the ten stations in Figure 1, were used to validate velocity calculations (Table 2). At most stations, the observed and modelled harmonic constants for tidal currents showed reasonable agreement. The mean differences between the observed and modelled velocities, for the semi-major and semi-minor axes, were 0.10 $m \cdot s^{-1}$ and 0.03 $m \cdot s^{-1}$, respectively, while the mean differences between ellipse inclination and phase were approximately 13º and 16º, respectively. At S5, S9, and S10, the differences were slightly larger, because the 200 m model resolution was insufficient to fully resolve the steep topography around these stations (Figure 1).

The simulated and observed potential temperatures and salinities coincided well, in both the surface and bottom layers, at high and low tides. The differences were less than 0.3 ℃ and 0.15 g / kg, at most stations.

Table 2. Observed/modelled tidal ellipse parameters for surface semidiurnal tides at the stations in Fig. 1. The tidal ellipse parameters include the semi-major (SEMA, $m \cdot s^{-1}$) and semi-minor (SEMI, $m \cdot s^{-1}$) axes, inclination (Inc, º) and phase (Pha, º). The mean absolute value differences and root mean squares (rms) for the observed and modelled tidal ellipse parameters were also calculated.

	Observed / Modelled Tidal Ellipse Parameters			
Stations	SEMA	SEMI	Inc	Pha
S1	0.36/0.29	0.08/0.01	43.93/54.48	59.35/49.76
S2	0.30/0.31	0.00/0.00	110.51/128.30	45.13/53.49
S3	0.30/0.35	0.02/0.02	54.14/63.94	30.07/52.81
S4	0.38/0.32	0.00/0.00	150.93/139.46	48.57/54.49
S5	0.24/0.45	0.01/0.05	128.91/98.52	15.49/58.45
S6	0.29/0.33	0.05/0.05	59.74/63.60	24.50/36.46
S7	0.45/0.43	0.02/0.04	123.41/148.62	40.69/59.13
S8	0.42/0.41	0.08/0.06	148.66/136.53	23.06/43.62
S9	1.09/0.70	0.01/0.11	97.24/101.48	65.39/58.35
S10	0.80/0.96	0.03/0.06	154.58/152.83	54.90/42.12
Mean dif	0.10	0.03	12.72	16.04
rms dif	0.12	0.03	9.31	11.09

Table 3. Observed / modelled Potential Temperature (PT) (℃) and Salinity (Sal) (g / kg) in surface (sur) and bottom (bot) layers, at high (H) and low (L) tides, at the stations

in Fig. 1. The mean absolute value differences and rms for the observed and modelled tidal ellipse parameters were also calculated.

	Observed / Modelled Potential Temperature				Observed / Modelled Salinity			
Stations	PT_H_sur	PT_H_bot	PT_L_sur	PT_L_bot	Sal_H_sur	Sal_H_bot	Sal_L_sur	Sal_L_bot
S1	26.41/26.82	26.41/26.83	27.52/27.56	27.52/27.57	30.27/30.35	30.27/30.34	28.83/29.67	29.53/29.66
S2	27.50/27.65	27.50/27.67	28.38/28.57	28.38/28.59	30.27/30.15	30.20/30.14	27.00/29.07	29.47/29.07
S3	26.84/26.68	26.84/26.69	26.90/27.04	26.90/27.02	30.56/30.60	30.59/30.60	30.51/30.39	30.56/30.41
S4	27.03/27.21	27.03/27.22	28.22/28.16	28.22/28.14	30.33/30.47	30.31/30.46	29.40/29.69	29.83/29.71
S5	26.57/25.96	25.60/25.97	26.54/26.63	26.15/26.27	30.60/30.78	30.91/30.78	30.69/30.64	30.71/30.71
S6	26.34/26.09	26.34/26.09	26.83/26.75	26.83/26.76	30.77/30.71	30.79/30.71	30.52/30.60	30.64/30.59
S7	26.57/26.36	25.60/26.29	27.68/27.55	27.17/27.03	30.86/30.78	31.05/30.84	30.43/30.27	30.47/30.56
S8	26.08/26.21	25.78/26.16	27.21/27.14	26.01/26.41	30.92/30.78	30.98/30.79	30.57/30.48	30.78/30.76
S9	26.01/25.76	25.59/25.77	26.99/26.39	26.33/26.16	30.81/30.80	30.90/30.81	30.47/30.68	30.61/30.79
S10	25.89/25.77	25.54/25.78	25.86/25.85	25.64/25.82	30.96/30.80	31.01/30.80	30.90/30.81	30.98/30.82
Mean dif	0.25	0.31	0.14	0.15	0.10	0.12	0.40	0.13
rms dif	0.15	0.17	0.17	0.10	0.05	0.07	0.63	0.11

4.2 Surface drift

Surface Lagrangian drift experiments were carried out in October 2012 (Figure 2 (a)). The drifter was tethered to a nylon cross drogue, centred at a 3-m depth, and the black square in the middle bay in the figure indicates the initial release location. The drifter was released on 18 Oct 2012, at 10:41 UTC (high tide), 0:30 UTC (maximum ebb), 4:30 UTC (low) and 7:30 UTC (maximum flood), respectively (Figure 2).

The drift trajectories for the first 13 h were used to verify the hydrodynamic and particle tracking model, in which labelled particles were tracked at different tidal phases. Although the M_2 semidiurnal tidal constituent was predominant in JZB (Ding, 1992), the simulated drifter deviated from the observed surface drifter trajectories due to minor hydrodynamic differences. Thus, with the same M_2 semidiurnal tidal constituent, another five principal tidal constituents—S_2, N_2, K_1, O_1, P_1—were specified at open boundaries. The five harmonic elevation constants were derived from the Oregon State University global inverse tidal model (TPXO7.0; available from http://volkov.oce.orst.edu/tides/) (Egbert and Erofeeva, 2002; Egbert et al., 1995). Meteorological observations at the initial drifter positions showed that the wind speed was generally < 2.0 m·s^{-1} during the surface Lagrangian drifter experiments and that the Dagu River discharge in October was reduced to approximately 20% of the summer maximum—thus, the effects of wind and density were neglected.

The modelled and observed drifter trajectories roughly coincided (Figure 2). Because the mean modelled ocean current bias was approximately 0.10 ms^{-1} (Table 2), the simulated particle trajectories could accumulate at least 4.68 km after 13 h. The mean differences between modelled and observed final drifter locations were ~ 1.33 km at high tide, 11.23 km at ebb tide, 0.69 km at low tide, and 3.36 km at flood tide. One reason for the large difference at ebb tide may be that the model resolution could not adequately simulate either nearshore progress or the large gradient ocean current around Outer Bay mouth at maximum ebb tide. At ebb tide, the surface drifter moved to Outer Bay quickly, and the particle approached too close to the coastline, thus causing the modelled and observed drifter trajectories to separate.

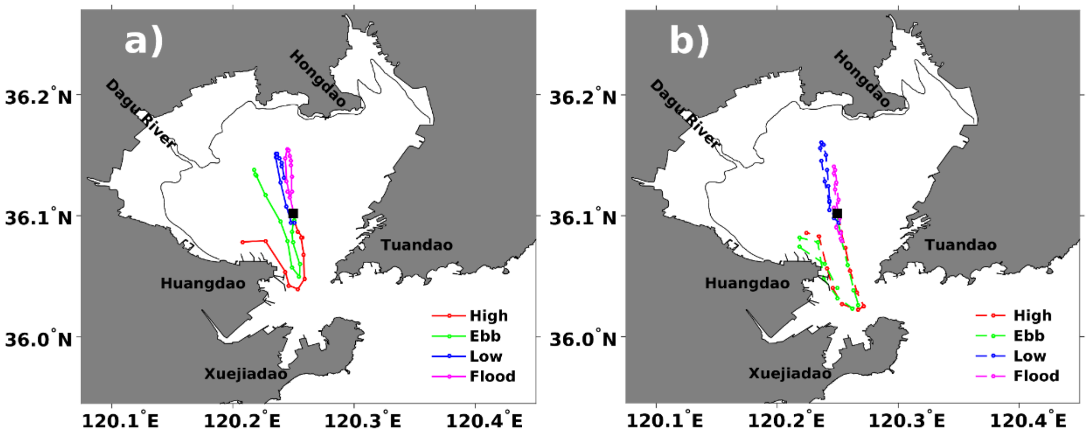

Figure 2. *Surface drifter (a) observed and (b) simulated trajectories, for four typical tidal phases. The solid black square marks the initial release location. The solid lines represent surface drifter observed trajectories, while the dashed lines represent simulated labelled particles trajectories for the surface layer.*

5 Results

5.1 Full LRV in the tide-wind-density system

The full LRV in the tide-wind-density system has been shown to depend highly on the initial tidal phases and has complex, 3D structures, consistent with the Lagrangian mean theory (Liu et al., 2012; Feng et al., 2008). In the tide-wind-density system, the Lagrangian residual transport velocity was similar to that in the tidal system, in which a large, counter-clockwise eddy dominated Inner Bay (Liu et al., 2012). As the large, counter-clockwise eddy in the Inner Bay was the key phenomenon of the full LRV, it has been indicated using lines with large arrows, in Figure 3.

Regarding the depth-averaged, full LRV, the dominant large eddy in Inner Bay clearly moved synchronously with the initial tidal phases (Figure 3), with its centre moving across half of Inner Bay. At high tide, the counter clockwise eddy flowed westward in the N half of Inner Bay, before turning SE around the Dagu River mouth and then merging in the middle bay to form an eddy (Figure 3(a)). During ebb tides, the eddy centre moved S towards the Inner Bay mouth, and became slightly smaller (Figure 3(b)), while by low tide, the eddy was at its smallest, and its centre was located at the

Inner Bay mouth. The eddy was found to flow along the E coastline and turn E into the northern Inner Bay, before flowing to the SE, along the Daguhe Channel, and merging around the Inner Bay mouth (Figure 3(c)), During flood tides, the flow pattern was similar to that determined for the ebb tide, although the eddy increased in size, and its centre moved to the N, below middle Inner Bay (Figure 3(d)).

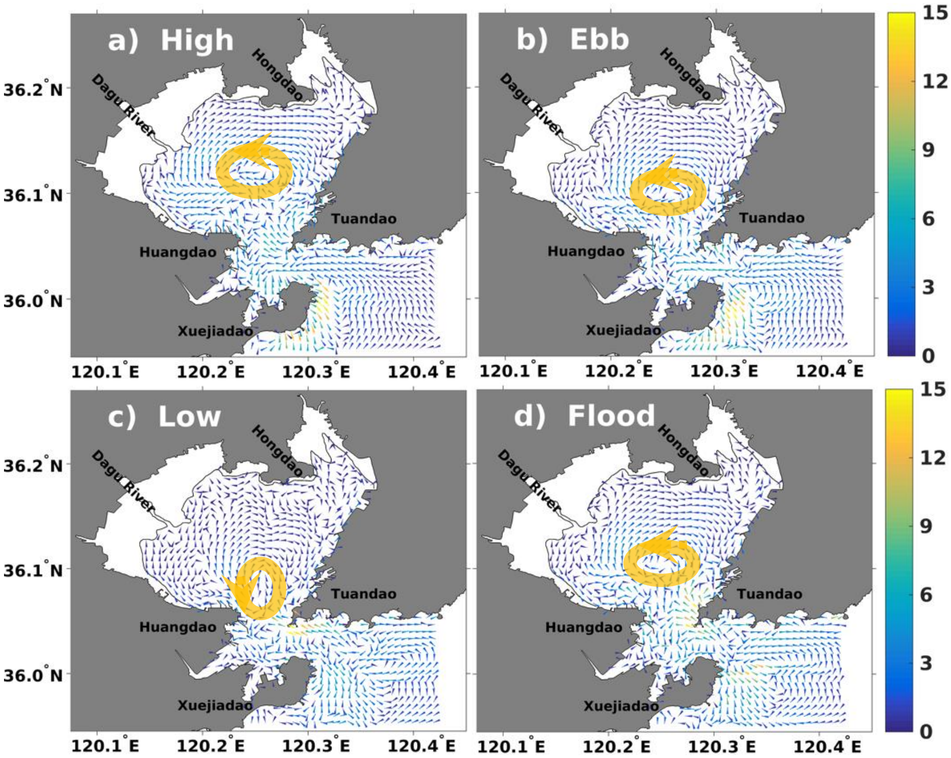

Figure 3. *The depth-averaged, full LRV for the tide-wind-density system at different initial tidal phases, when the labelled water parcels were released at: (a) high tide; (b) maximum ebb tide; (c) low tide; (d) maximum flood tide. The colours indicate magnitude (cm·s*$^{-1}$*), and arrows indicate direction.*

Flow patterns for the vertically sheared, tidally averaged full LRV were found to be quite different (Figure 4). In the surface layer, the full LRV eddy flowed westward in the N Inner Bay, before turning SE. The westward part of the eddy covered the whole of Inner Bay, apart from the SE part of the eddy which flowed through the SW part of the bay (Figure 4(a)); in the middle layer, a large counter-clockwise eddy dominated Inner Bay (Figure 4(b)), while in the bottom layer, the full LRV flowed to the N in the western half of Inner Bay, and to the E in its eastern half (Figure 4(c)).

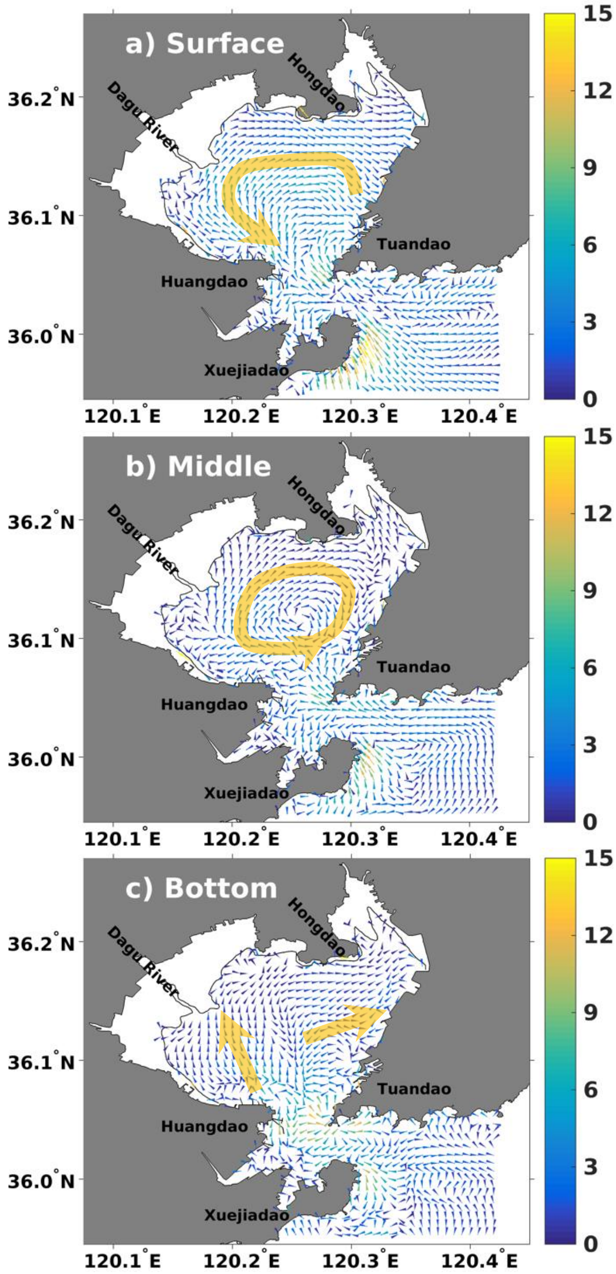

Figure 4. *Tidally averaged LRV for different sigma layers in the JZB tide-wind-density system. The Lagrangian residual velocities were deployed at the initial positions of the labelled water parcels. Colours indicate magnitude ($cm{\cdot}s^{-1}$), and arrows indicate direction.*

5.2 Wind-driven LRV

The wind-driven full LRV was found to consist mainly of two remarkable branches, which moved and stretched with the tidal phases (Figure 5). One branch flowed clockwise in the W part of the bay, and the other branch flowed counter-clockwise in its NE. Magnitudes were < 3 $cm{\cdot}s^{-1}$. At high tide, as the branches receded back to the coastal shallow regions around the tidal flats (Figure 5(a)); then during the ebb, the two branches became extended (Figure 5(b)), so that, by low tide, the two branch extensions reached their maximums, covering the whole of Inner Bay. At this point, the clockwise branch covered the SW quarter of Inner Bay, while the counter-clockwise branch dominated its left three-quarters (Figure 5(c)), before receding in area again, once flood tide movements re-commenced (Figure 5d).

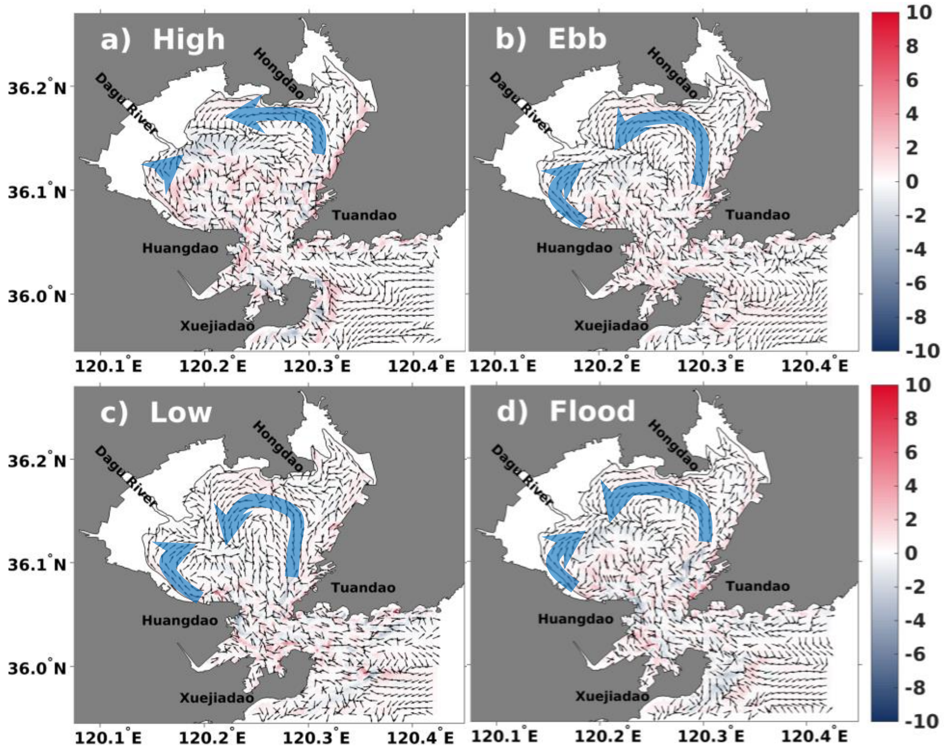

Figure 5. *Wind-driven, depth-averaged full LRV in the tide-wind-density system at different initial tidal phases when the labelled water parcels were released at (a) high tide; (b) maximum ebb tide; (c) low tide; (d) maximum flood tide. Colours indicate magnitude (cm·s^{-1}), and arrows indicate direction. Positive values indicate that the wind effect has the same direction as the tide-wind-density driven full LRV, and vice versa.*

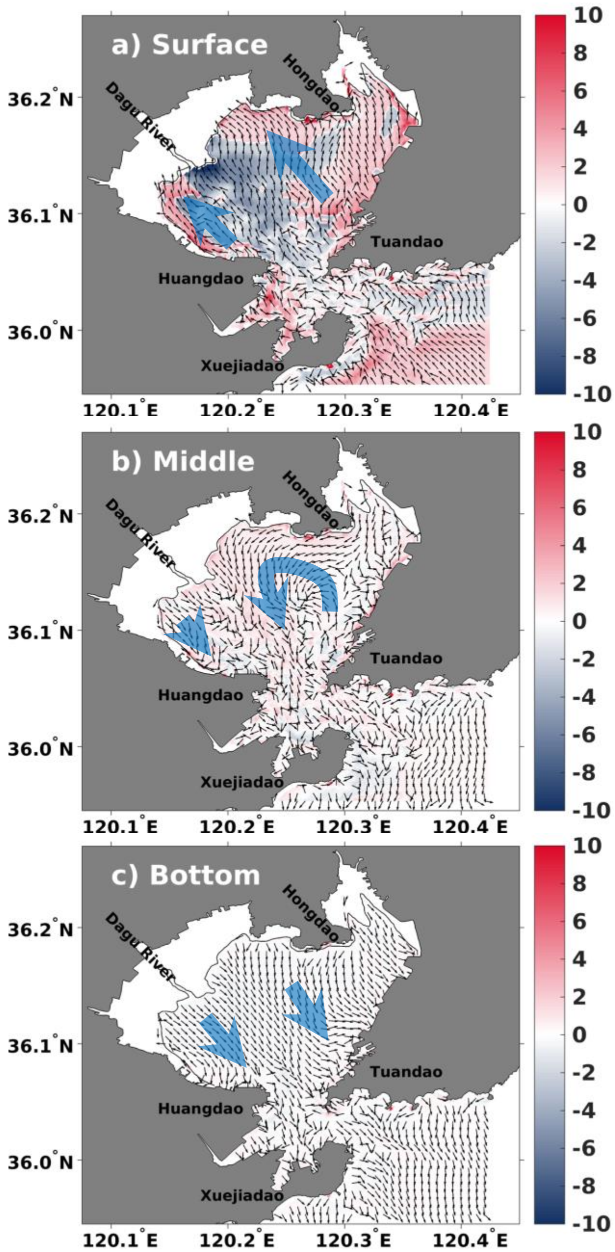

Figure 6. *Wind-driven, tidally averaged full LRV for different sigma layers in the tide-wind-density system. Full LRV were deployed at the initial positions of the labelled water parcels. Colours indicate magnitude (cm·s^{-1}), and arrows indicate direction. Positive values indicate that the wind effect has the same direction as the tide-wind-density driven full LRV, and vice versa.*

The wind-driven, tidally averaged full LRV was found to flow downwind in the shallow upper layer, and upwind, to compensate, in the deeper bottom layer (Figure 6). In the surface layer, the wind-driven full LRV flowed downwind, enhancing the tide-wind-density driven full LRV in the NE shallows, but reducing the tide-wind-density driven full LRV along the Daguhe and Daoerhe Channels. Its magnitude reached as high as 4 cm·s^{-1} (Figure 6(a)). In the middle layer, the wind-driven full LRV formed counter-clockwise flows in the NE bay, and upwind flow in its west, while enhancing the tide-wind-density driven full LRV by < 3 cm·s^{-1} (Figure 6(b)). In the bottom layer, the wind-driven full LRV flowed upwind, and mainly played a negative role. The velocity flowed SE to the bay mouth to compensate, with magnitudes of < 2 cm·s^{-1} (Figure 6(c)).

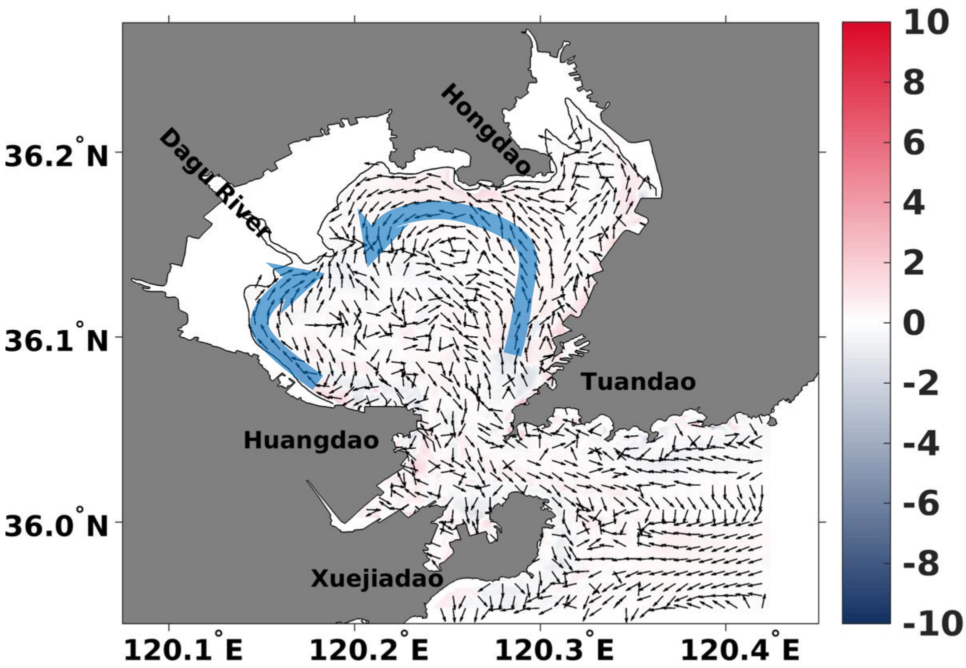

Figure 7. *Wind-driven, tidally depth-averaged Lagrangian residual transport velocity in the tide-wind-density system. The Lagrangian residual transport velocities started at the initial positions of the labelled water parcels. Colours indicate magnitude (cm·s^{-1}) and arrows indicate direction. Positive values indicate that the wind effect has the same direction as the tide-wind-density driven full LRV, and vice versa.*

Generally, wind enhanced the full LRV in the shallows, but weakened its velocity in deeper regions along the Daguhe and Daoerhe Channels in Inner Bay (Figure 7). In the tide-wind-density system, the tidally averaged, depth-averaged, wind-driven Lagrangian residual transport velocity flowed clockwise in the SW bay, and counter-clockwise in its NE, with the two areas divided by a line between the Dagu River mouth and bay mouth. The two branches then merged around the Dagu River mouth. The wind-driven, full LRV magnitude was mainly < 2 cm·s^{-1} and played a positive role in the Lagrangian residual flows.

In summary, the wind-driven full LRV in JZB has been found to be highly dependent on the initial tidal phases and to have complex, 3D structures. Wind-driven flow patterns were similar, although the main branches could move across half of Inner Bay at different initial tidal phases (Figure 5). Wind enhanced the full LRV in the shallows, but weakened its velocity in the deeper regions, along the Daguhe and Daoerhe Channels of Inner Bay.

5.3 Density-driven LRV

The density-driven LRV was shown to have two significant branches, which varied with the tidal phase water movements of Inner Bay (Figure 8). One clockwise flow occupied most of W Inner Bay, at low tide, before almost disappearing at high tide, while the other was represented by a W flow that could extend to nearly all the N Inner Bay at high tide but almost disappeared at low tide. At high tide, the density-driven, full LRV formed a strong W flow in the middle of Inner Bay. A narrow stream flowed E in northern Inner Bay (Figure 8(a)), and when ebbing, the density-driven full LRV flowed towards the bay mouth in the middle, deeper region. A semicircle-like, density-driven Lagrangian residual circulation flowed clockwise through the northern shallow region along the tidal flats (Figure 8(b)). At low tide, the density-driven, full LRV flowed clockwise along the tidal flats, and the clockwise flows dominated W Inner Bay, while the full LRV, flowing towards the Inner Bay mouth, nearly disappeared (Figure 8 (c)). At flood tide, the density-driven full LRV was similar to its ebb tide form (Figure 8(d)).

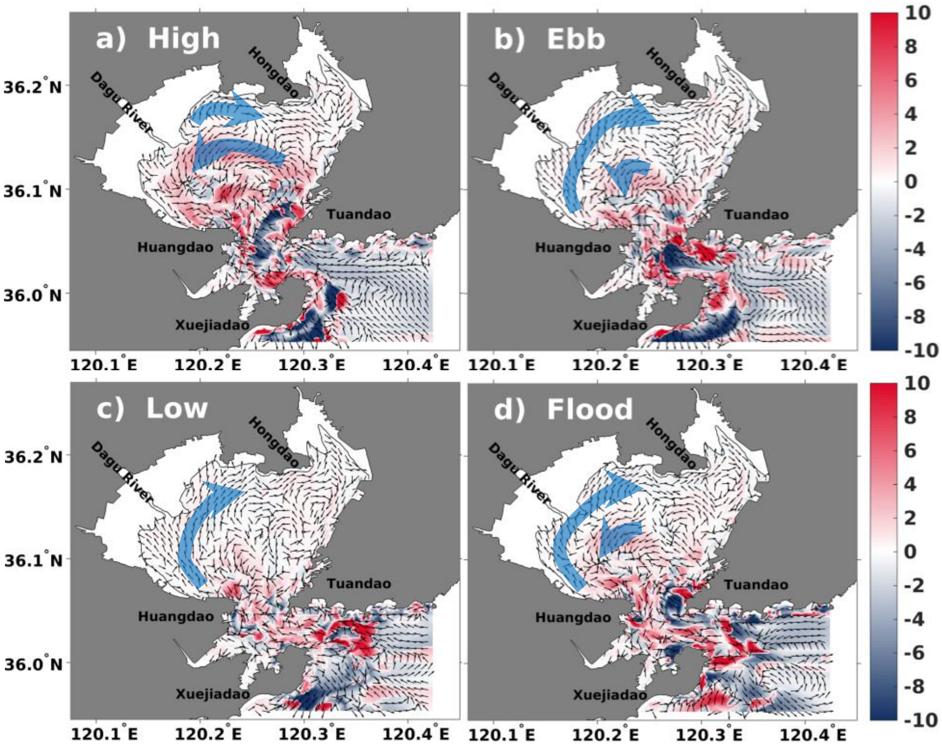

Figure 8. *Density-driven, depth-averaged full LRV in the tide-wind-density system when the labelled water parcels were released at different initial tidal phases: (a) high tide; (b) maximum ebb tide; (c) low tide; (d) maximum flood tide. Colours indicate magnitude (cm·s^{-1}), and arrows indicate direction. Positive*

values indicate that the density effect has the same direction as the tide-wind-density driven full LRV, and vice versa.

In contrast to the SE wind-driven full LRV, the density-driven full LRV generally flowed outward in the upper layer, and inward in the bottom layer (Figure 9). In the surface layer, the density-driven full LRV flowed towards the bay mouth, enhancing the tide-wind-density driven, full LRV by > 4 cm·s^{-1} in the middle bay (Figure 9(a)). In the middle layer, the full LRV still flowed towards the bay mouth in the middle bay but formed a semicircle-like, clockwise flow in the NE bay (Figure 9(b)), while in the bottom layer, the full LRV flowed NW (Figure 9(c)). Density generally enhanced the full LRV in the tide-wind-density system.

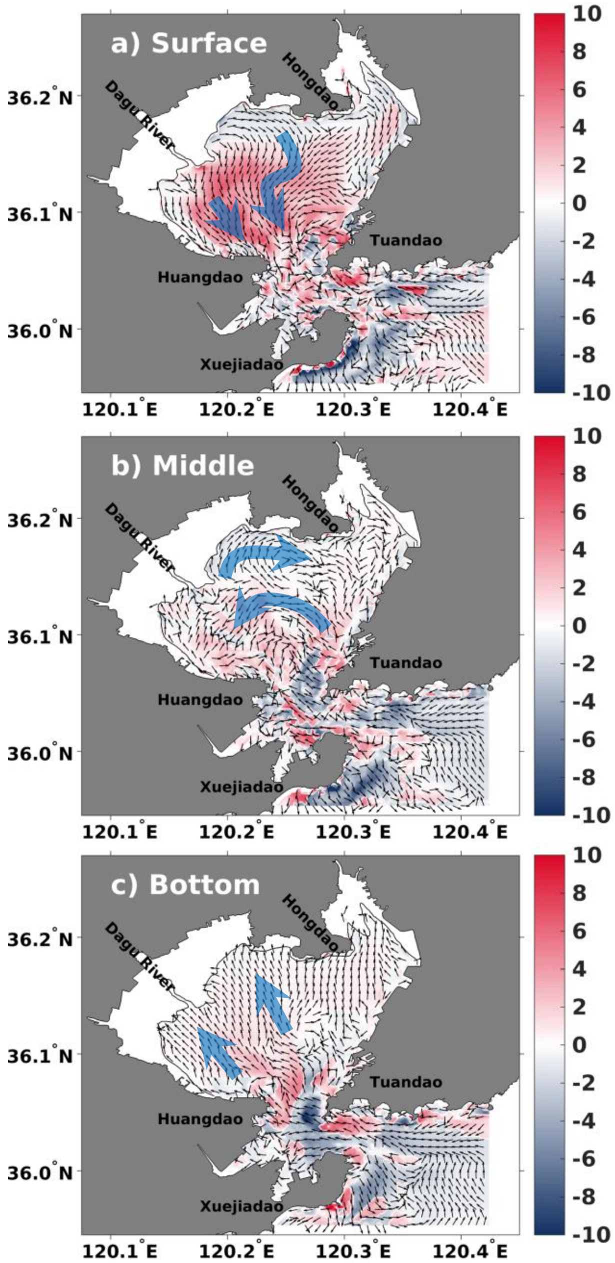

Figure 9. *Density-driven, tidally averaged full LRV on different sigma layers in the*

tide-wind-density system. Full LRV were deployed at the initial positions of the labelled water parcels. Colours indicate magnitude (cm·s^{-1}), and arrows indicate direction. Positive values mean that the density effect has the same direction as the tide-wind-density driven full LRV, and vice versa.

In the tide–wind–density system, the density-driven Lagrangian residual transport velocity mainly flowed counter-clockwise in middle Inner Bay, and to the E in the northern Inner Bay (Figure 10). In Outer Bay, density mainly drove seawater to flow into the bay. The effect of density mainly enhanced the tide-wind-density driven Lagrangian residual velocity in Inner Bay, while reducing velocities in Outer Bay. Flow rates reached up to 4 cm·s^{-1}, in most regions.

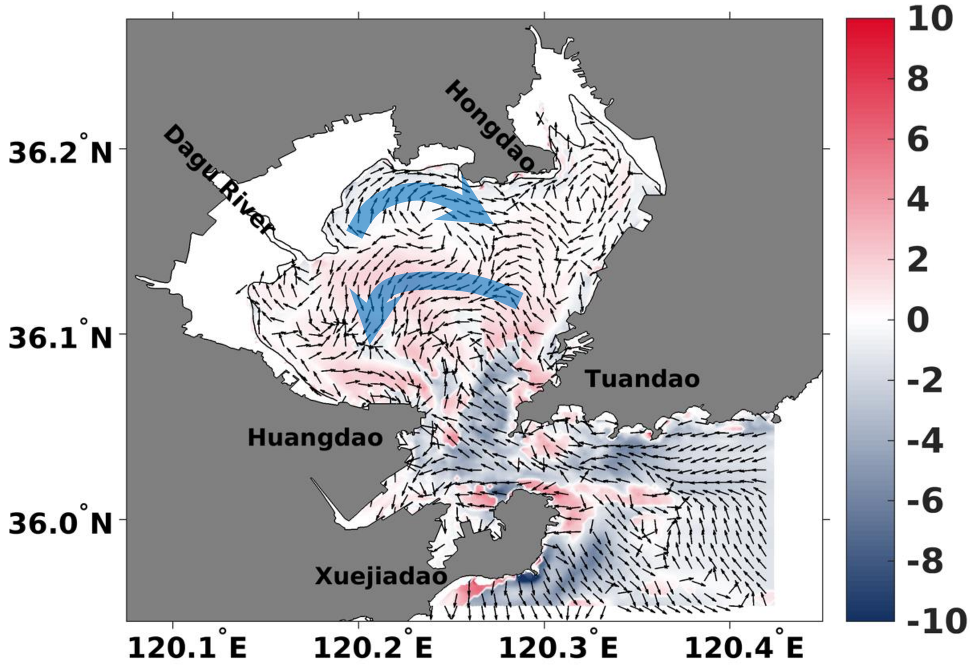

Figure 10. *Density-driven, tidally depth-averaged Lagrangian residual transport velocity in the tide–wind–density system. Lagrangian residual transport velocities were deployed at the initial positions of the labelled water parcels. Colours indicate magnitude (cm·s^{-1}), and arrows indicate direction. Positive values mean that the density effect has the same direction as the tide-wind-density driven full LRV, and vice versa.*

5.4 Comparison with ERV

The distinct difference between the wind- and density-driven residual velocities was that the depth-averaged ERV (Figure 11) was not related to the initial tidal phase, while the full LRV was highly dependent on it (Figs 5 and 8). The wind-driven ERV (Figure 11-1) showed a laterally sheared, three-layer circulation pattern that was similar to that of the wind-driven, full LRV (Figure 5). However, the wind-driven ERV did not vary with tidal phase, while the density-driven ERV (Figure 11-2) was quite different from the density-driven full LRV (Figure 8). Moreover, for the wind-driven ERV, the density-driven ERV did not vary with the tidal phase.

The observed trajectories in Figure 2 show the time dependence on the initial tidal phases. The different net displacements across the four tidal phases indicated that the full LRV would be highly reliant on the initial time.

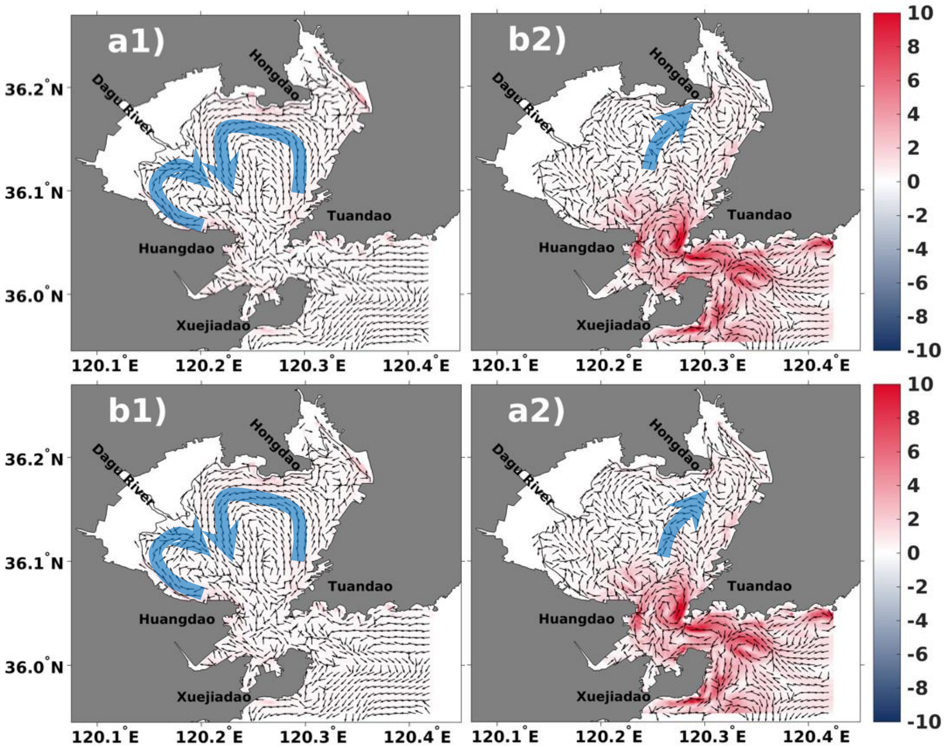

Figure 11. *The wind- (left 1) and density- (right 2) driven, depth-averaged ERV in the tide-wind-density system at: (a) high tide; (b) low tide. The other two tidal phases have been omitted, as their ERVs were identical to that for high tide. Colours indicate magnitude (cm·s^{-1}), and arrows indicate direction. Positive values mean that the density effect has the same direction as the tide-wind-density driven ERV and vice versa.*

6 Dynamics governing the general spatial pattern of full LRV

Ekman ($\mathrm{E_k}$), Kelvin (K_e) and Wedderburn (W) numbers have been used to analyse the flow patterns and dynamics of the wind- and density-driven flows qualitatively. The wind-driven flow pattern, under the effects of the earth's rotation, depended on the ratio of the maximum basin depth, h_{max}, to the Ekman depth, d (d $=$ $\sqrt{2\mathrm{A_z}/\mathrm{f}}$) (Winant, 2004; Sanay and Valle-Levinson, 2005). The function $\mathrm{h}_{max}/\mathrm{d}$ is related to the usual Ekman number definition $E_k = A_z/\left(f {h_{max}}^2\right)$ by $\mathrm{h}_{max}/\mathrm{d} =$

$1/\sqrt{2\mathrm{E_k}}$. The density-driven flow pattern, as influenced by basin width, friction and the Earth's rotation, could be investigated as a function of the Ekman ($\mathrm{E_k}$) and Kelvin (K_e) numbers (Valle-Levinson, 2008). Alterations to the density-driven flow caused by wind-driven flow were explored in the $\mathrm{E_k}$ and W parameter spaces, through an examination of the lateral structure of the resulting exchange flows (Reyes-Hernández and Valle-Levinson, 2010; Jia and Li, 2012).

To compare with the numerical results, semi-analytical solutions for wind- and density-driven flow were also obtained, across the NE-SW section (indicated by the dashed line between Huangdao and Hongdao in Figure 1, which represented the main features of the topography and flow patterns of the tide-, wind- and density-driven, full LRV. The section was perpendicular to the wind direction, and its average depth was found to be approximately the same as the mean depth of the whole JZB. The downwind direction looking into the bay from the bay mouth was negative, and momentum terms were decomposed in the section.

6.1 Dynamics for the role of wind

Earth's rotational influence on wind-driven flow was characterized as a function of $\mathrm{h}_{max}/\mathrm{d}$ (Winant, 2004; Sanay and Valle-Levinson, 2005). Winant (2004) presented a 3D, linear, barotropic model to describe the wind-driven flow in an elongated basin of arbitrary depth distribution, on an f plane. For $\mathrm{h}_{max}/\mathrm{d}$ values > 3, the along-channel flow showed that axial asymmetries and transverse circulations played an important role. When $\mathrm{h}_{max}/\mathrm{d}$ remained ≤ 1, the pattern of wind-driven circulation could be described as a non-rotating system (Csanady, 1982; Wong, 1994), so JZB was considered to approximate a non-rotating system, since its $\mathrm{h}_{max}/\mathrm{d}$ values approached 1 in most Inner Bay regions. The Inner Bay cross-section was almost triangular, suggesting that the wind may have led to a laterally sheared, three-layer circulation, as was derived in the analytical solutions, with downwind currents on the shallow shoals and upwind flows in the central, deeper channel (Figure 7). Vertically, the wind drove downwind flow, with upwind countercurrents active in the bottom layers (Figure 6) (Csanady, 1982; Wong, 1994; Winant, 2004).

Wind-driven flows can be obtained from the semi-analytical solution of the dynamic balance between the pressure gradient, frictional effects and Coriolis forces (Eqs 10–11) (e.g., Winant, 2004; Narváez and Valle-Levinson, 2008). If u_w and v_w are the components of wind-driven flow, $\vec{u}_w$, $\vec{u}_w = u_w + i\, v_w$, $N = \frac{\partial\eta}{\partial x} + i\frac{\partial\eta}{\partial y}$ describes the water level gradient, and $t_s = t_s^x + it_s^y$ denotes the direction of the wind stress in the complex plane, as shown in Eq. (10):

$$\vec{u}_w = t_s \frac{\sinh\left(\alpha(z'+h')\right)}{\alpha \cosh(\alpha h')} - \frac{N}{\alpha^2}\left(1 - \frac{\cosh(\alpha z')}{\cosh(\alpha h')}\right) \tag{10}$$

where $\vec{u}_w$, h' and z' represent the non-dimensional, across-section flow, depth, and across-section vertical coordinate, respectively. $\alpha^2 = 2iD_E{}'^{-2}$, for which $D_E{}'$ denotes the non-dimensional Ekman layer depth $(2A_z/fh_{m0}{}^2)^{1/2}$, where A_z stands for the vertical eddy viscosity (1×10^{-2} $m^2 \cdot s^{-1}$), h_{m0} indicates the non-dimensional, maximum across-section water depth, and $\frac{\partial\eta}{\partial x}$ represents the simulated, tidally averaged, across-section water level gradient in our model.

To compare the semi-analytical results with our numerically simulated wind-driven flows, the analytical solution was dimensionalised, as shown in (11):

$$\vec{u}_d = \frac{\tau h_m}{\rho A_z}\vec{u}_w \tag{11}$$

where $\vec{u}_d$ denotes the dimensionalised, semi-analytical solution of wind-driven flow, ρ represents sea water density ($kg \cdot m^{-3}$), τ refers to wind stress (P_a), and h_m indicates the maximum across-section water column depth (m).

The semi-analytical solution (Figure 12 (a)) was quite consistent with the simulated, tidally averaged, wind-driven full LRV in the tide-wind-density system (Figure 12 (b)), with Inner Bay found to behave similarly to a NW–SE oriented lake. Across the section, the wind-driven full LRV was found to flow downwind in the thin surface layer (< 2 m), and upwind, in a compensating countercurrent, below the surface layer, in the tide-wind-density system.

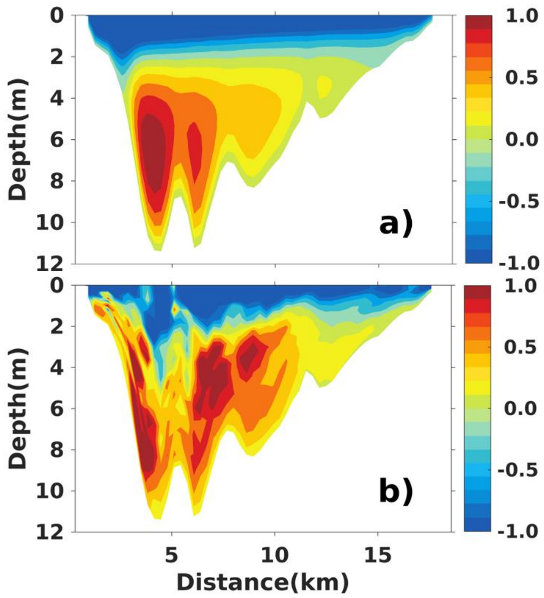

Figure 12. *(a) Semi-analytical solutions for wind-driven flow (as depicted by Winant [2004] under homogeneous conditions, the cross-sectional mean depth (5 m)*

segregated downwind and upwind flows); (b) wind-driven, full LRV in the tide-wind-density system. The section is that indicated by the dashed line between Huangdao and Hongdao in Figure 1. Negative values denote areas of upwind flow (unit: cm·s^{-1}).

6.2 Dynamics for the role of density

The flow pattern of the density-driven flow influenced by basin width, friction, and the Earth's rotation, could be classified as a function of the Ekman (E_k) and Kelvin (K_e) numbers (Valle-Levinson, 2008; Reyes-Hernández and Valle-Levinson, 2010). Valle-Levinson (2008) studied the lateral current structure of a density-driven exchange flow in an estuary, using an analytic model. The lateral structure of the density-driven flow, as influenced by basin width, friction, and Earth's rotation, was investigated as a function of the Ekman (E_k) and Kelvin (K_e) numbers. For a large E_k ($E_k > 1$), the laterally sheared exchange flow, which consisted of seaward flow over the shallow regions and inflow from the bottom to the surface in the middle of the deeper channel, was independent of basin width (K_e). Under moderate friction (0.01 < E_k < 0.1), the exchange pattern was both horizontally and vertically sheared, for all widths. The exchange pattern described the horizontal inflow in the channel and outflow over the shallows, and the outflow at the surface and inflow underneath, vertically. Horizontally sheared patterns are best defined for wide basins—that is, those with a high K_e.

In JZB, the Ekman number, E_k, was > 0.2, in most Inner Bay regions, which meant that the area experienced moderate to high friction conditions. The Kelvin number,K_e, was > 1. A lower E_k and a high K_e meant that the density-driven flow was both vertically and horizontally sheared in JZB. Vertically, the density-driven flow moved seaward in the upper layer, and landward in the middle and bottom layers, in Inner Bay (Figure 9). Laterally, the density-driven Lagrangian residual transport velocity flowed outward in the SW regions, and inward in the E Inner Bay (Figure 10).

A semi-analytical solution was generated for density-driven flow, based on a dynamic balance between the baroclinic pressure gradient, the barotropic pressure gradient, friction and Coriolis forces (e.g., Kasai et al., 2000; Valle-Levinson, 2003; Valle-Levinson, 2008). In a right-handed coordinate system (x, y, z), where x points seaward, y points across the basin, and z points upward, the non-tidal (or steady) momentum balance can be represented by a set of two differential equations, as shown in (12):

$$\begin{aligned} -\mathrm{fv} &= -\mathrm{g}\frac{\partial \eta}{\partial x} + \frac{g}{\rho}\frac{\partial \rho}{\partial x}\mathrm{z} + A_z\frac{\partial^2 u}{\partial z^2} \\ fu &= -g\frac{\partial \eta}{\partial y} + \frac{g}{\rho}\frac{\partial \rho}{\partial y}z + A_z\frac{\partial^2 v}{\partial z^2} \end{aligned} \quad (12)$$

Eq. (12) may be solved for a complex velocity, $w = u + i\,v$, where ($i^2 = -1$) is the imaginary number, as shown in Eq. (13):

$$\mathrm{w(z) = g\,N\,F_1(z) + F_2(z)} \tag{13}$$

where N represents sea level slope from the barotropic pressure gradient ($\partial\eta/\,\partial x + i\,\partial\eta/\,\partial y$), and functions $\mathrm{F_1}$ and $\mathrm{F_2}$ depict the vertical structure of barotropic (from sea level slope) and baroclinic (from density gradient) flow contributions, respectively, as described in Eq. (14):

$$\begin{gathered} F_1 = \frac{i}{f}\left[1 - \frac{\cosh(\alpha z)}{\cosh(\alpha h)}\right] \\ F_2 = \frac{iD}{f\alpha}\left[(e^{\alpha z} - \alpha z) - \left(e^{-\alpha h} + \alpha h\right)\frac{\cosh(\alpha z)}{\cosh(\alpha h)}\right] \end{gathered} \tag{14}$$

where D equals $g/\rho(\partial\rho/\,\partial x + i\,\partial\rho/\,\partial y)$, and is independent of depth; the parameter α equals $(1 + i)/d$, where d is the Ekman layer depth $(2A_z/f)^{1/2}$. Eq. (14) was obtained by assuming no stress at the surface ($\partial F_1/\,\partial z = \partial F_2/\,\partial z = 0$, at $\mathrm{z} = 0$), and no slip at the bottom ($F_1 = 0$ and $F_2 = 0$, at $z = -h$). The sea level slope, N, and a density gradient, D (that is dynamically consistent with N), were prescribed, as described by Valle-Levinson et al. (2003). Section width, B, = 15 km, and bathymetric variation across domain h was established using the real section topography shown in Figure 1.

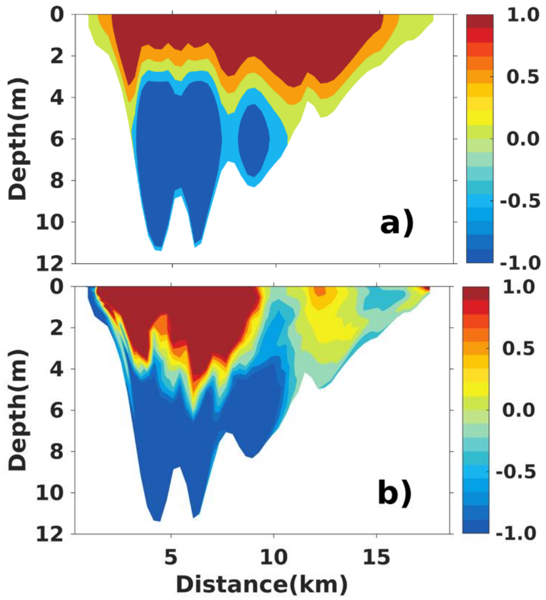

Figure 13. *(a) Semi-analytical solution for density-driven flows (as depicted by Valle-Levinson [2008]); (b) density-driven, full LRV in the tide-wind-density system. The section is that indicated by the dashed line between Huangdao and Hongdao in Figure 1. Negative areas denote upwind flows (unit: cm·s^{-1}).*

In JZB, the semi-analytical solution (Figure 13 (a)) depicted the main features of the tidally averaged, density-driven Lagrangian residual flow across the section in the tide-wind-density system (Figure 13 (b)). The density-driven, full LRV flowed into the bay along the deep Daguhe and Daoerhe Channels, and out via surface layers.

7 Diagnosis analysis for intra-tidal variations of full LRV

Further insights into the wind- and density-driven circulation in JZB were gained by conducting diagnostic analysis of the momentum balance. The momentum terms across the section delineated in Figure 1, were calculated, together with depth-integrated momentum terms. The momentum balances at maximum high and low tides were taken as examples, to explore the mechanism of intra-tidal variations in full LRV, because the wind- and density- driven, full LRVs were quite different at high tide and low tide.

We integrated arbitrary momentum terms (denoted as ψ) along particle trajectories (denoted as S), as $\int_S \psi ds$, where ds denotes a piecewise trajectory over one model time step. The difference in the momentum terms among the tide-wind-density, tide-wind and tide-density systems could be regarded as the effect of wind and density in the tide-wind-density system. The POM employs a sigma coordinate in the vertical direction, so that the momentum equation was as shown in Eqs (15)–(17) (Mellor, 2004):

$$\frac{\partial UD}{\partial t} + \overbrace{\frac{\partial U^2D}{\partial x} + \frac{\partial UVD}{\partial y} + \frac{\partial U\omega}{\partial \sigma}}^{nonlinear\ advection} \overbrace{-fVD}^{Coriolis\ force} + \overbrace{gD\frac{\partial \eta}{\partial x}}^{barotropic\ pressure\ gradient} +$$

$$\overbrace{\frac{gD^2}{\rho_o}\int_\sigma^0 \left[\frac{\partial \rho'}{\partial x} - \frac{\sigma'}{D}\frac{\partial D}{\partial x}\frac{\partial \rho'}{\partial \sigma'}\right] d\sigma'}^{baroclinic\ pressure\ gradient} = \overbrace{\frac{\partial}{\partial \sigma}\left[\frac{A_z}{D}\frac{\partial U}{\partial \sigma}\right] + \frac{\partial}{\partial x}\left(2hA_M\frac{\partial U}{\partial x}\right) + \frac{\partial}{\partial y}\left(hA_M\left(\frac{\partial U}{\partial y} + \frac{\partial V}{\partial x}\right)\right)}^{viscosity} \quad (15)$$

Surface boundary condition could be represented as shown in (16):

$$\frac{A_z}{D}\left(\frac{\partial U}{\partial \sigma}, \frac{\partial V}{\partial \sigma}\right) = \overbrace{-(< wu(0) >, < wv(0) >)}^{wind\ stress}, \sigma \to 0 \quad (16)$$

while bottom boundary condition could be described as in (17):

$$\frac{A_z}{D}\left(\frac{\partial U}{\partial \sigma}, \frac{\partial V}{\partial \sigma}\right) = \overbrace{C_z[U^2 + V^2]^{1/2}(U, V)}^{bottom\ friction}, \sigma \to -1 \quad (17)$$

where, x, y and z are conventional Cartesian coordinates; U, V and ω represent the velocities in the sigma coordinate; $D = h + \eta$ represents total water depth; $\sigma = \frac{z-\eta}{h+\eta}$ represents the sigma coordinate, which ranges from 0 at the surface to -1 at the bottom, and ρ_o and ρ' stand for the reference water density and density perturbation, respectively; A_M represents the horizontal viscosity coefficient, while $wu(0)$ and $wv(0)$ stand for wind momentum fluxes at the surface; C_z represents the bottom friction coefficient, and then the integrated momentum term was divided by total depth, *D*, along each trajectory.

7.1 Lagrangian momentum balance analysis for wind

Analysis of the cross-section momentum terms also showed a rough balance between the barotropic pressure gradient due to the elevation setup and viscosity (Figure 14). As the Rossby radius of deformation in JZB was approximately 100 km—and the typical JZB horizontal scale was approximately 25 km—Coriolis forces were not really important in JZB. In an idealized rectangular estuary, the axial wind-driven flow consists of a vertically sheared, two-layer circulation, and has been interpreted in terms of the competition between wind stress and the barotropic pressure gradient, due to the sea level setup (Garvine, 1985; Janzen and Wong, 2002; Jia and Li, 2012). The wind modifies the momentum balance through the barotropic pressure gradient, due to the surface slope setup and viscosity. In our case, it has been shown that the local SE wind could change the vertical viscosity structure, leading to a significant increase in surface layer viscosity (Gong et al., 2009), and that, under an SE wind, the sea level decreased from the NW Dagu River mouth to the SE Inner Bay mouth, as water piled up in NW upper Inner Bay (Valle-Levinson et al., 2001; Guo and Valle-Levinson, 2008). In our case, wind accumulated water in the NW direction, and driven an upwind barotropic pressure gradient (Figure 15 (c)).

Vertically, viscosity was negative in the surface layer, except around the Daguhe Channel, and positive viscosity forced water to flow outward, beneath the surface layer, during both high and low tides (Figure 14). The barotropic pressure gradient was positive across the section at low tide, while at high tide, it was mostly negative in the Daguhe Channel surface layer. At low tide, a positive barotropic pressure gradient, together with the viscosity, forced the wind-driven full LRV to flow upwind along the Daguhe Channel and under the surface layer (Figs 5(c) and 14-2), while in the surface region of high negative viscosity, the negative viscosity overcame the positive barotropic pressure gradient, forcing the wind-driven full LRV to flow downwind. At high tide, viscosity was higher than the barotropic pressure gradient, in bilateral shallow regions, but the balance was unclear across most parts of the section—leaving the wind-driven full LRV disordered (Figs 5(a) and 14-1).

Horizontally, depth-averaged, wind-driven flow developed mainly as the result of competition between imposed, depth-integrated viscosity, the pressure gradient, wind stress and bottom friction (Figure 15), while the respective influences of nonlinear advection and the baroclinic pressure gradient were not crucial, for the SE wind-driven full LRV. At high tide, viscosity had advantages in only the shallow regions below Hongdao, while elsewhere in the region, nonlinear advection, viscosity, wind stress, and the barotropic and baroclinic pressure gradients competed—leaving the wind-driven full LRV disordered (Figs 5(a) and 15-1). At low tide, over the shallows below Hongdao and the E Huangdao shore—where the pressure gradient effect was relatively weak—viscosity and wind stress overcame the pressure gradient, to drive the downwind current., allowing the corresponding bottom stress to balance the imposed residual disordered momentum term (Figs 5(c) and 15-2).

In the deep Daguhe and Daoerhe channels, the adverse wind viscosity and pressure gradient had a relatively greater influence, which overwhelmed the wind stress, to drive an upwind flow. The flow was upwind as the bottom stress and wind stress were balanced by the viscosity and the pressure gradient. Passing from the shallows to the deep channels, the bottom stress switched signs as the wind-driven flow direction changed.

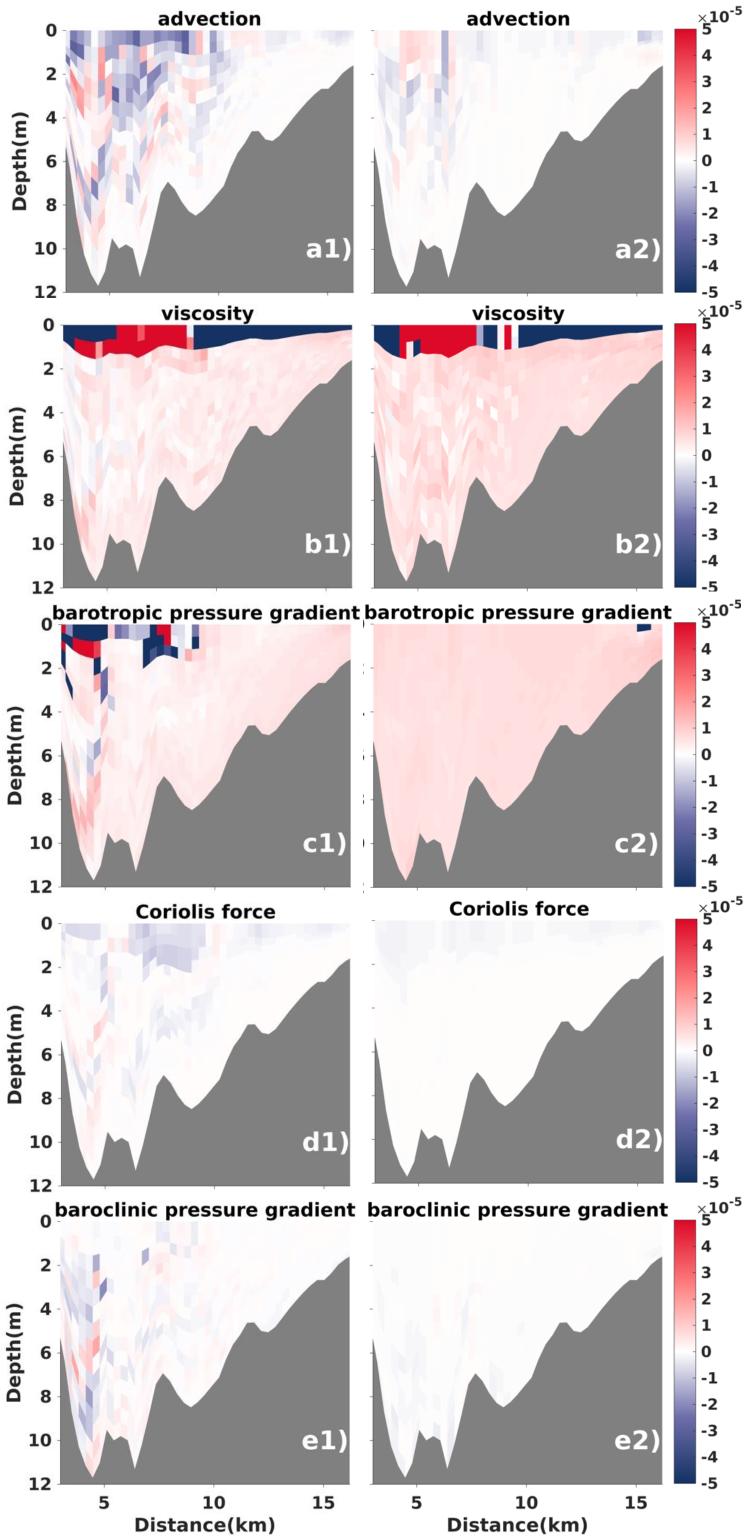

Figure 14. *Momentum balance across the section for wind-driven full LRV in the JZB tide-wind-density system, at: 1) high tide; 2) low tide. The section is that depicted by the dashed line between Huangdao and Hongdao in Figure 1. Momentum terms integrated along particle trajectories: (a) Tidally averaged, nonlinear advection; (b) viscosity; (c) barotropic pressure gradient; (d) Coriolis forces; (e) baroclinic pressure gradient. Unit:* $m^2 \cdot s^{-2}$.

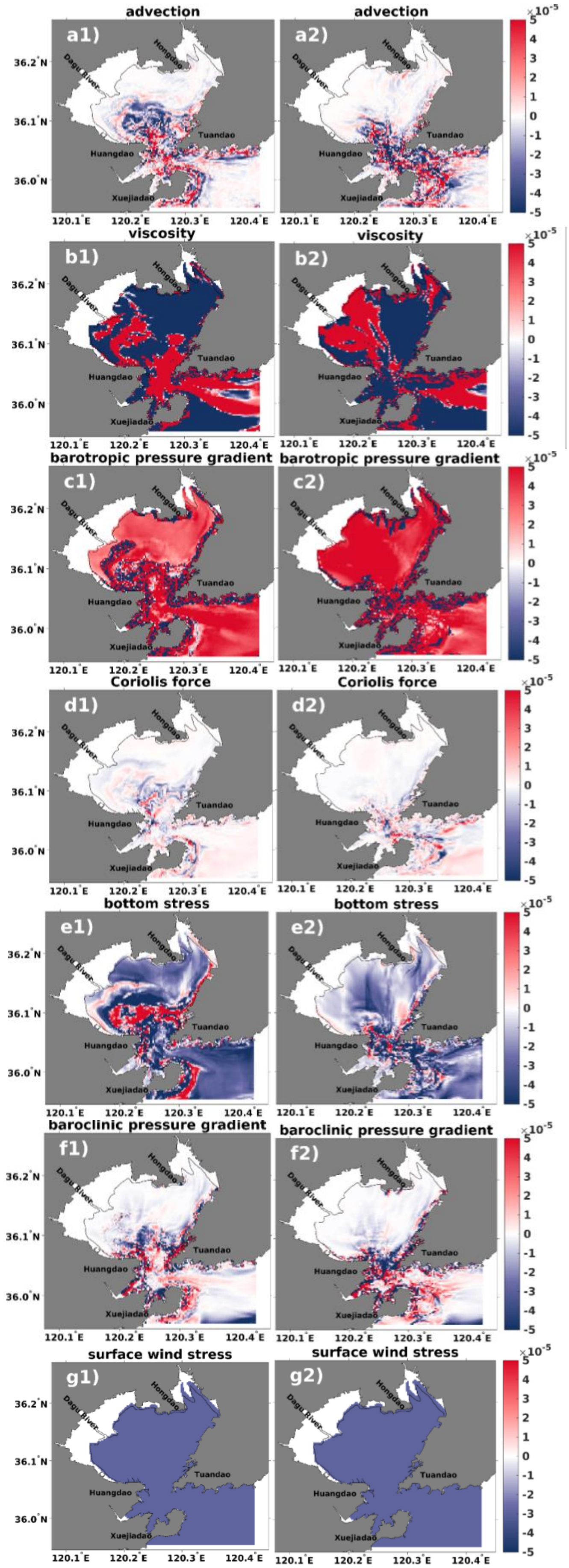
advection
a1)
a2)
viscosity
b1)
b2)
barotropic pressure gradient
c1)
c2)
Coriolis force
d1)
d2)
bottom stress
e1)
e2)
baroclinic pressure gradient
f1)
f2)
surface wind stress
g1)
g2)
Hongdao
Dagu River
Tuandao
Huangdao
Xuejiadao
36.2°N
36.1°N
36.0°N
120.1°E
120.2°E
120.3°E
120.4°E
$\times10^{-5}$
5
4
3
2
1
0
-1
-2
-3
-4
-5

Figure 15. *Distribution of momentum terms for wind-driven full LRV at 1) high tide and 2) low tide, perpendicular to the section: (a) depth-integrated nonlinear advection; (b) viscosity; (c) barotropic pressure gradient; (d) Coriolis forces; (e) bottom stress; (f) baroclinic pressure gradient; (g) surface wind stress. The section is that depicted by the dashed line between Huangdao and Hongdao in Figure 1. Unit:* $m^2 \cdot s^{-2}$*, and wind is in the SE direction.*

7.2 Lagrangian momentum balance analysis for density

Momentum balance across the section occurred amongst the baroclinic and barotropic pressure gradients, viscosity, Coriolis forces and advection (Figure 16).

Vertically, we found that viscosity was the main momentum parameter driving outward, density-driven flow in the surface layer (Figs 9 and 16). Below this layer, the baroclinic pressure gradient overcame the other momentum terms, to drive water flow into the bay, with the relatively weak advection, barotropic pressure gradient and Coriolis forces acting against each other. At high tide, positive viscosity, nonlinear advection, barotropic pressure gradient and Coriolis forces overwhelmed the negative baroclinic pressure gradient, so that the density-driven full LRV flowed upwind in the NE part of the section, while in the SW part, near the deep channels, the negative viscosity and baroclinic pressure gradient forced Lagrangian flow downwind. At low tide, negative viscosity, and the barotropic and baroclinic pressure gradients drove downwind, density-driven Lagrangian flow along the Huangdao coastline, while positive viscosity, nonlinear advection and Coriolis forces drove Lagrangian flow upwind in the NE part of the section.

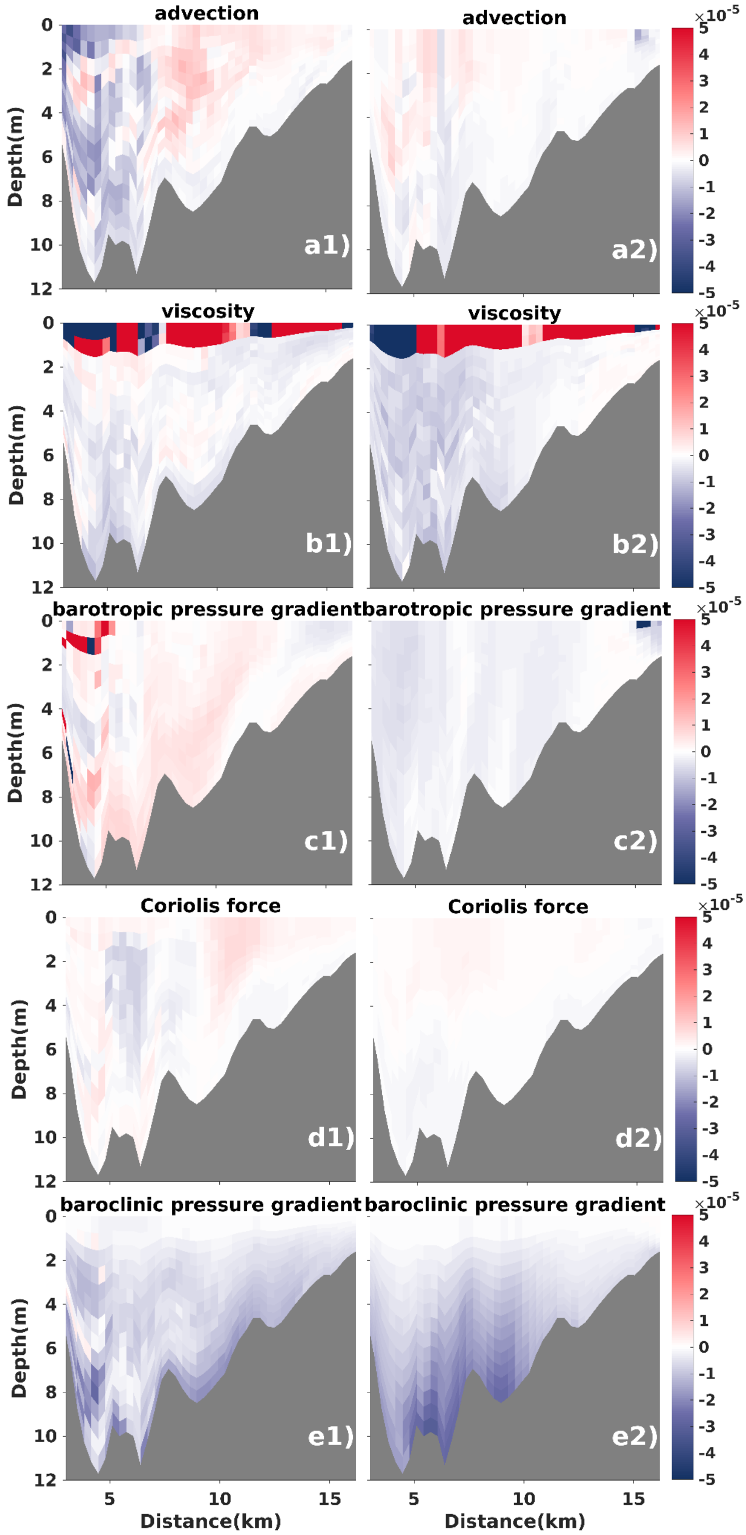

Figure 16. *Momentum balance in the JZB tide-wind-density system across the section, for density-driven full LRV, at 1) high tide, and 2) low tide, illustrating momentum terms integrated along particle trajectories: (a) tidally averaged, non-linear advection; (b) viscosity; (c) barotropic pressure gradient; (d) Coriolis forces; (e) baroclinic pressure gradient. Unit:* $m^2 \cdot s^{-2}$*. The section is that depicted by the dashed line between Huangdao and Hongdao in Figure 1.*

Horizontally, the momentum terms cannot all be neglected around the bay mouth, while only the viscosity and the barotropic and baroclinic pressure gradients were important in the Inner Bay top shallow region (Figure 17). At high tide (Figs 8a and 17-1), the positive viscosity and barotropic pressure gradient overcame the negative baroclinic pressure gradient, and the density-driven full LRV flowed SE, while at low tide (Figs 8c and 17-2), the barotropic pressure gradient became negative in the western part of Inner Bay. The negative barotropic and baroclinic pressure gradients were stronger than the positive viscosity, and forced the NW, density-driven full LRV.

In summary, viscosity and the baroclinic pressure gradient were found to be the main drivers for density-driven, full LRV, depending upon initial tidal phases, while the barotropic pressure gradient and nonlinear advection were also important. Water parcel trajectories differed during different tidal phases, so that the momentum terms and balances also differed.

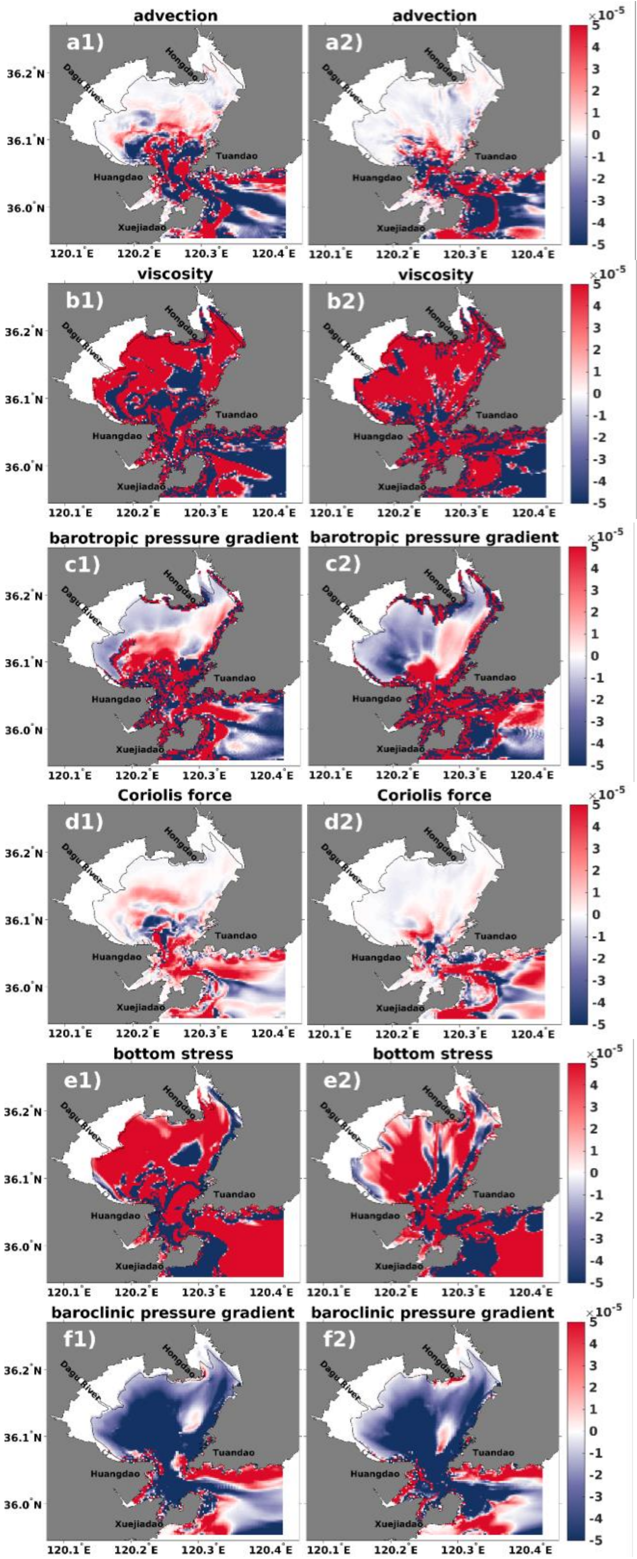

Figure 17. *Distribution of momentum terms for density-driven full LRV at 1) high tide, and 2) low tide, perpendicular to the section: (a) depth-integrated nonlinear advection; (b) viscosity; (c) barotropic pressure gradient; (d) Coriolis forces; (e) bottom stress; (f) baroclinic pressure gradient. The section is that depicted by the dashed line between Huangdao and Hongdao in Figure 1. Unit:* $m^2 \cdot$

s^{-2}.

8 Competition between wind and density effects on residual velocities

It has been reported that a tide-wind-density driven, full LRV is similar to a tide-driven full LRV (Liu et al., 2012). This indicates that in the tide-wind-density system, tides determine the residual circulation patterns, while wind and density only apply influence.

In JZB, the effects of wind and density on residual velocities were comparable—and countered each other. The full LRV patterns in different layers throughout both Inner Bay (Figs 6 and 9), and the cross section (Figs 12 and 13), showed that the effect of the SE wind acted against density, for the full LRV. Competition among tide-, wind- and density-driven flows showed complex, 3D structures. In the upper layer, above the western channels, the outward tide and density-driven flow overcame the wind-driven flow, while the magnitudes of the tide- and wind-driven flows were stronger in the middle layer. In the surface layer of the eastern shallow region, the downwind tide and wind-driven full LRV overwhelmed the density-driven outward full LRV. In the bottom layer, since the tide- and wind-driven flows were weaker than the density-driven flow, the tide-wind-density driven full LRV flowed inwards.

Alteration of density-driven flow by the wind-driven flow have been explored in the E_k and W parameter spaces, through examination of the lateral structures of the resulting exchange flows (Reyes-Hernández and Valle-Levinson, 2010), and it has been found that wind-driven circulation was dominant when W > 1, whereas gravitational circulation was dominant when W < 1 (Geyer, 1997). Across the section in JZB, W = ~ 1, and $E_k < 1$. The effects of density and wind were comparable, although the wind's role was relatively weak.

In the tide-wind-density system, the SE wind acted against density, on the full LRV. Wind stresses produced enhancement, inversion or damping, of density-driven flows, by altering viscosity and the pressure gradients—and by momentum transfer from wind drag—while viscosity and the barotropic pressure gradient were greatly enhanced by wind stress (Figs 14 and 15). Density affected both viscosity and the baroclinic pressure gradient (Figs 16 and 17), and since density-driven viscosity and the baroclinic pressure gradient played opposing roles in wind-driven viscosity and the barotropic pressure gradient, the SE wind effectively acted against density. Overall though, these momentum terms exerted weaker effects than did tidal advection, because wind and density did not alter the patterns of the tide-driven full LRV, in the tide-wind-density system.

9 Conclusions

In this paper, we have focused on the effects of wind and density on residual circulation in a tide-dominated bay, from the Lagrangian view. In the tide-wind-density system, both the wind- and the density-driven, full LRVs were highly dependent on the initial tidal phases, and exhibited complex, 3D structures.

Basic wind- and density-driven, full LRV patterns were consistent with simplified semi-analytical solutions, although, compared with the wind- or density-driven ERV, the time dependence of wind- and density-driven full LRVs in the tide-wind-density system was a very distinct feature. Given an initial tidal phase in a tide-dominated area, the wind-driven full LRV was different, even with a constant wind force. This suggested that, when analysing wind and density effects on residual circulation in tidally energetic waters, 3D structures and initial tidal phases should both be considered.

Momentum balance analysis, integrated along particle trajectories, was used to explain the time dependence of the wind- and density-driven full LRVs. This analysis showed that intra-tidal viscosity variation was the main force causing time dependence in the wind-driven full LRV, while the barotropic and baroclinic pressure gradients, together with viscosity, caused intra-tidal variation in the density-driven full LRV.

Acknowledgments

This study was financially supported by the Special Fund for Public Welfare Industry (Oceanography; grant No. 200805011). Dr Guangliang Liu thanks the Youth Foundation of the Shandong Academy of Sciences (grant No. 2019QN0026). All observational data behind the plots and all additional model data can be found at https://github.com/guangliangliu/ts_wind_jiaozhoubay, while the full data set is also available by contacting the corresponding author, Dr Zhe Liu (zliu@ouc.edu.cn).

References

Cai, Z.Y., Liu, Z., Guo, X.Y., Gao, H.W. and Wang, Q. (2014), Influences of intratidal variations in density field on the subtidal currents: Implication from a synchronized observation by multiships and a diagnostic calculation, J. Geophys. Res., 119 (3), 2017-2033, http://dx.doi.org/10.1002/2013JC009262.

Chen, D.X. (1992), Marine Atlas of Bohai Sea, Yellow Sea, East China Sea: Hydrology, China Ocean Press, Beijing (in Chinese).

Chen, J.R., Chen, X.E., Yu, H.M., Yan, Y.W., Shan., S.L. and Zhao, J. (2011), Three dimensional high resolution numerical study of the tide and tidal current in the

Jiaozhou Bay, Period Ocean Univ. China, 41, 29–35 (in Chinese, with English abstract).
Chen, Y., Jiang, W.X., Chen, X., Wang, T. and Bian, C.W. (2017), Laboratory experiment on the 3D tide-induced Lagrangian residual current using the PIV technique, Ocean Dyn., 67(12), 1567–1576, http://doi:10.1007/s10236-017-1108-6.
Chen, Z.S., Wang, W.H. and Wu, S.Y (2007), China Bay Introduction (in Chinese with English Abstract), Ocean Press, Beijing, 1-583.
Cheng, R.T., Feng, S.Z. and Xi, P.G. (1986), On Lagrangian residual ellipse, in Physics of Shallow Estuaries and Bays, vol. 16, edited by J. van de Kreeke, pp. 102-113, American Geophysical Union, Washington, D. C., http://doi.org/10.1029/LN016p0102
Cheng, R.T. and Casulli V. (1982), On Lagrangian residual currents with applications in south San Francisco Bay, California, Water Resour. Res., 18(6), 1652–1662, doi:10.1029/WR018i006p01652.
Csanady, G.T. (1982), Circulation in the Coastal Ocean. D. Reidel, 279 pp.
Cui, Y.X., Jiang, W.S. and Deng, F.J. (2018), 3D numerical computation of the tidally induced Lagrangian residual current in an idealized bay, Ocean Dyn., 18(8), 1–18, http://doi:10.1007/s10236-018-01243-1.
Cui, Y.X., Jiang, W.S. and Zhang J.H. (2019), Improved Numerical Computing Method for the 3D Tidally Induced Lagrangian Residual Current and Its Application in a Model Bay with a Longitudinal Topography, J. Ocean Univ. China, 18(6), 1235–1246, doi:10.1007/s11802-019-4216-8.
Delhez, E.J.M. (1996), On the residual advection of passive constituents, J. Mar. Syst., 8 (3-4), 147-169. http://dx.doi.org/10.1016/0924-7963(96)00004-8.
Deng, F.J., Jiang, W.S. and Feng, S.Z. (2017), The nonlinear effects of the eddy viscosity and the bottom friction on the Lagrangian residual velocity in a narrow model bay, Ocean Dyn., 67(9), 1105–1118, http://doi:10.1007/s10236-017-1076-x.
Deng, F.J., Jiang, W.S., Valle-Levinson, A. and Feng, S.Z. (2019), 3D Modal Solution for Tidally Induced Lagrangian Residual Velocity with Variations in Eddy Viscosity and Bathymetry in a Narrow Model Bay, J. Ocean Univ. China, 18(1), 69–79, http://doi:10.1007/s11802-019-3773-1.
Ding, W.L. (1992), Tides and tidal currents (in Chinese), in Ecology and Living Resources of Jiaozhou Bay, edited by R.Y. Liu, Science Press, Beijing, pp. 39-57.
Editorial Board of Annals in China (1993), Jiaozhou Bay Annals of bays in China (in Chinese), Ocean Press, Beijing.

Egbert, G. D., Bennett, A. F. and Foreman, M. G. G. (1995), TOPEX/Poseidon tides estimated using a global inverse model, J. Geophys. Res.: Oceans, 99(C12), 24821–24852.

Egbert, G. D. and Erofeeva, S. Y. (2002), Efficient inverse modeling of barotropic ocean tides, J. Atmos. Ocean. Tech., 19(2), 183–204.

Fairall, C. W., Bradley, E. F., Hare, J. E., Grachev, A.A. and Edson, J.B. (2003), Bulk parameterization of air sea fluxes: Updates and verification for the COARE Algorithm, Journal of Climate, 16(4), 571–591.

Fairall, C. W., Bradley, E. F., Rogers, D. P., Edson, J. B. and Young, G. S. (1996a), Bulk parameterization of air-sea fluxes for Tropical Ocean- Global Atmosphere Coupled-Ocean Atmosphere Response Experiment, J. Geophys. Res., 101(C2), 3747–3764.

Feng, S.Z., Cheng, R.T. and Xi, P.G. (1986a), On tide-induced lagrangian residual current and residual transport: 1. Lagrangian residual current, Water Resour. Res., 22 (12), 1623-1634, http://dx.doi.org/10.1029/WR022i012p01623.

Feng, S.Z., Cheng, R.T. and Xi, P.G. (1986b), On tide-induced Lagrangian residual current and residual transport: 2. Residual transport with application in south San Francisco Bay, California, Water Resour. Res., 22 (12), 1635-1646, http://dx.doi.org/10.1029/WR022i012p01635.

Feng, S.Z. (1987), A three-dimensional weakly nonlinear model of tide-induced Lagrangian residual current and mass-transport, with an application to the Bohai Sea, in Three-dimensional Models of Marine and Estuarine Dynamics, edited by J.C.J. Nihourl and B.M. Jamart, Elsevier Oceanography Series, Amsterdam, pp. 471–488, https://doi.org/10.1016/S0422-9894(08)70463-X.

Feng, S.Z. (1990), On the Lagrangian residual velocity and the mass-transport in a multi- frequency oscillatory system, in Residual Currents and Long-term Transport, Coastal and Estuarine Studies, edited by R.T. Cheng, Springer, Berlin, pp. 34–48, https://doi.org/10.1007/978-1-4613-9061-9_4.

Feng, S.Z., Ju, L. and Jiang, W.S. (2008), A Lagrangian mean theory on coastal sea circulation with inter-tidal transports I. Fundamentals, Acta. Oceanol. Sin., 27 (6), 1-16, https://doi.org/10.3969/j.issn.0253-505X.2008.06.001.

Fung, I.Y., Harrison, D.E. and Lacis, A.A. (1984) On the variability of the net longwave radiation at the ocean surface, Rev. Geophys. Space Phys., 22, 177-193.

Garvine, R.W. (1985), A simple model of estuarine subtidal fluctuations forced by local and remote wind stress, J. Geophys. Res., 90 (C6), 11945-11948, http://dx.doi.org/10.1029/JC090iC06p11945.

Garvine, R.W. (1995), A dynamical system for classifying buoyant coastal discharges, Cont. Shelf Res., 15 (13), 1585–1596, https://doi.org/10.1016/0278-4343(94)00065-U.

Geyer, W.R. (1997), Influence of wind on dynamics and flushing of shallow estuaries, Estuar. Coast. Shelf Sci., 44 (6), 713-722, https://doi.org/10.1006/ecss.1996.0140.

Geyer, W.R. and MacCready, P. (2014), The Estuarine Circulation, Annu. Rev. Fluid Mech., 46, 175-197, http://dx.doi.org/10.1146/annurev-fluid-010313-141302.

Gong, W., Shen, J. and Hong, B. (2009), The influence of wind on the water age in the tidal Rappahannock River, Mar. Environ. Res., 68 (4), 203–216, http://doi:10.1016/j.marenvres.2009.06.008.

Guo, X.Y. and Valle-Levinson, A. (2008), Wind effects on the lateral structure of density-driven circulation in Chesapeake Bay, Cont. Shelf Res., 28 (17), 2450–2471, http://doi:10.1016/j.csr.2008.06.008.

Ianniello, J.P. (1977), Tidally induced residual currents in estuaries of constant breadth and depth, J. Mar. Res., 35, 755-786.

Janzen, C.D. and Wong, K.C. (2002), Wind-forced dynamics at the estuary-shelf interface of a large coastal plain estuary, J. Geophys. Res., 107, 3138, doi:10.1029/2001JC000959.

Jia, P. and Li, M. (2012), Dynamics of wind-driven circulation in a shallow lagoon with strong horizontal density gradient, J. Geophys. Res., 117, C05013, http://dx.doi.org/10.1029/2011JC007475.

Jiang, W.S. and Feng, S.Z. (2011), Analytical solution for the tidally induced Lagrangian residual current in a narrow bay, Ocean Dyn., 61 (4), 543-558, http://dx.doi.org/10.1007/s10236-011-0381-z.

Jiang, W.S. and Feng, S.Z. (2014), 3D analytical solution to the tidally induced Lagrangian residual current equations in a narrow bay, Ocean Dyn., 64 (8), 1073-1091, http://dx.doi.org/10.1007/s10236-014-0738-1.

Jiang, D.J. and Wang, X.L. (2013), Variation of Runoff Volume in the Dagu River Basin in the Jiaodong Peninsula, Arid Zone Res., 30(6), 965-972.

Kasai, A., Hill, A.E., Fujiwara, T. and Simpson, J.H. (2000), Effect of the Earth's rotation on the circulation in regions of freshwater influence, J. Geophys. Res., 105 (C7), 16961-16969. http://dx.doi.org/10.1029/2000JC900058.

Klingbeil, K., Becherer, J., Schulz, E., et al. (2019), Thickness-Weighted Averaging in Tidal Estuaries and the Vertical Distribution of the Eulerian Residual Transport, J. Phys. Oceanogr., 49(7), 1809–1826. doi: 10.1175/JPO-D-18-0083.1

Lange, X. and Burchard, H. (2019), The relative importance of wind straining and gravitational forcing in driving exchange flows in tidally energetic estuaries, J. Phys. Oceanogr., JPO–D–18–0014.1–42, http://doi:10.1175/JPO-D-18-0014.1

Li, Y. and Li, M. (2011), Effects of winds on stratification and circulation in a partially mixed estuary, J. Geophys. Res., 116, C12012, http://10.1029/2010JC006893.

Liu, G.L., Liu, Z., Gao, H.W., Gao, Z.X. and Feng, S.Z. (2012), Simulation of the Lagrangian tide-induced residual velocity in a tide-dominated coastal system: a case study of Jiaozhou Bay, China, Ocean Dyn., 62 (10), 1443-1456, http://dx.doi.org/10.1007/s10236-012-0577-x.

Liu, G.L., Liu, Z. and Gao, H.W. (2013), Analysis of Intra-Tidal Variation of Sea Temperature in Jiaozhou Bay in Summer Based on Synchronous Observation (in Chinese, with English abstract), Period. Ocean Univ. China, 4, 85-93.

Lin, L., Liu, Z., Xie, L.A., Gao, H.W., Cai, Z.Y., Chen, Z.Y. and Zhao, J.Z. (2015), Dynamics governing the response of tidal current along the mouth of Jiaozhou Bay to land reclamation, J. Geophys. Res., 120(4), 2958–2972, http://doi.org/10.1002/2014JC010434.

Mellor, G.L. and Yamada, T. (1982), Development of a turbulence closure model for geophysical fluid problems, Rev. Geophys., 20(4), 851– 875.

Mellor, G.L. (2004), Users guide for a three-dimensional, primitive equation, numerical ocean model, report, 8-10 pp., Program in Atmos. and Oceanic Sci., Princeton Univ., Princeton, N. J.

Monismith, S. (1986), An experimental study of the upwelling response of stratified reservoirs to surface shear stress, J. Fluid Mech., 171, 407-439, doi:10.1017/S0022112086001507

Muller, H., Blanke, B., Dumas, F., Lekien, F. and Mariette, V. (2009), Estimating the Lagrangian residual circulation in the Iroise Sea, J. Mar. Syst., 78 (Supplement), S17-S36, https://doi.org/10.1016/j.jmarsys.2009.01.008.

Muller, H., Blanke, B., Dumas, F. and Mariette, V. (2010), Identification of typical scenarios for the surface Lagrangian residual circulation in the Iroise Sea, J. Geophys. Res., 115, C07008, http://dx.doi.org/10.1029/2009JC005834.

Narváez, D.A. and Valle-Levinson, A. (2008), Transverse structure of wind-driven flow at the entrance to an estuary: Nansemond River, J. Geophys. Res., 113, C09004, http://dx.doi.org/10.1029/2008JC004770.

Paulson, C.A. and Simpson, J.J. (1977), Irradiance measurements in the upper ocean, J. Phys. Oceanogr., 7, 953–956.

Pritchard, D. W. (1952), Salinity distribution and circulation in the Chesapeake Bay estuarine system, J. Mar. Res., 11, 106–123.

Quan, Q., Mao, X.Y. and Jiang, W.S. (2014), Numerical computation of the tidally induced Lagrangian residual current in a model bay, Ocean Dyn., 64 (4), 471-486, http://dx.doi.org/10.1007/s10236-014-0696-7.

Reyes-Hernández, C. and Valle-Levinson, A. (2010), Wind modifications to density-driven flows in semienclosed, rotating basins, J. Phys. Oceanogr., 40, 1473-1487, http://dx.doi.org/10.1175/2010JPO4230.1.

Sanay, R. and Valle-Levinson A. (2005), Wind-Induced Circulation in Semienclosed Homogeneous, Rotating Basins, J. Phys. Oceanogr., 35(12), 2520–2531, doi:10.1175/JPO2831.1.

Smagorinsky, J., Manabe, S. and Holloway, JL.Jr. (1965), Numerical results from a nine-level general circulation model of the atmosphere, Mon. Weather Rev., 93(12), 727–768.

Valle-Levinson, A., Wong, K.-C. and Bosley, K.T. (2001), Observations of the wind-induced exchange at the entrance to Chesapeake Bay, J. Mar. Rea., 59 (3), 391–416, http://doi:10.1357/002224001762842253.

Valle-Levinson, A., Reyes, C. and Sanay, R. (2003), Effects of Bathymetry, Friction, and Rotation on Estuary-Ocean Exchange, J. Phys. Oceanogr., 33, 2375-2393, http://dx.doi.org/10.1175/1520-0485(2003)033<2375:EOBFAR>2.0.CO;2.

Valle-Levinson, A. (2008), Density-driven exchange flow in terms of the Kelvin and Ekman numbers, J. Geophys. Res., 113, C04001, http://dx.doi.org/10.1029/2007JC004144.

Wang, H., Su, Z.Q., Feng, S.Z. and Sun W.X. (1993), A three-dimensional numerical calculation of the wind-driven thermohaline and tide-induced Lagrangian residual current in the Bohai Sea, Acta Oceanol. Sin., 12(2), 169–182.

Wang, Q. and Gao, H.W. (2003), Study on Wind Stress and Air-sea Exchange over Coastal Waters of Qingdao (in Chinese, with English abstract), Adv. Mar. Sci., 21 (1), 12-20.

Wang, T., Jiang, W.S., Chen, X. and Feng, S.Z. (2013), Acquisition of the tide-induced Lagrangian residual current field by the PIV technique in the laboratory, Ocean Dyn., 63 (11), 1181-1188, http://dx.doi.org/10.1007/s10236-013-0654-9.

Winant, C.D. (2004), Three-dimensional wind-driven flow in an elongated, rotating basin, J. Phys. Oceanogr., 34, 462-476, http://dx.doi.org/10.1175/1520-0485(2004)034<0462:TWFIAE>2.0.CO;2.

Winant, C.D. (2008), Three-dimensional residual tidal circulation in an elongated, rotating basin, J. Phys. Oceanogr., 38(6), 1278–1295, doi:10.1175/2007JPO3819.1.

Wong, K.-C. (1994), On the nature of transverse variability in a coastal plain estuary, J. Geophys. Res., 99(C7), 14209–14222, doi:10.1029/94JC00861.

Xu, P., Mao, X.Y. and Jiang, W.S. (2016), Mapping tidal residual circulations in the outer Xiangshan Bay using a numerical model, J. Mar. Syst., 44 (3), 181-191, https://doi.org/10.1016/j.jmarsys.2015.10.002.

Zhang, J. (2007), Watersheds Nutrient Loss and Eutrophication of the Marine Recipients: A Case Study of the Jiaozhou Bay, China, Water, Air, & Soil Pollution: Focus, 7(6), 583–592, doi:10.1007/s11267-007-9130-1.

Zimmerman, J.T.F. (1979), On the Euler–Lagrange transformation and the Stokes' drift in the presence of oscillatory and residual currents, Deep-Sea Res., 26A, 505–520, https://doi.org/10.1016/0198-0149(79)90093-1.

Figure and Table Captions

Figure 1. *JZB bathymetry (m). The gridded region represents tidal flats. JZB can be divided into the Inner Bay and Outer Bay by the solid line between Tuandao and Huangdao. The bay channel connecting JZB to the Yellow Sea is located between Tuandao and Xuejiadao. The blue cross represents the Xiaomaidao meteorological observation station. The numbered white circles denote the sampling stations where synchronous observations were conducted during August 2009. The dashed line between Huangdao and Hongdao indicates the section used both for momentum balance analyses and to compare the simulated and analytical solutions for wind- and density-driven residual velocities discussed in Section 6.*

Figure 2. *Surface drifter (a) observed and (b) simulated trajectories, for four typical tidal phases. The solid black square marks the initial release location. The solid lines represent surface drifter observed trajectories, while the dashed lines represent simulated labelled particles trajectories for the surface layer.*

Figure 3. *The depth-averaged, full LRV for the tide-wind-density system at different initial tidal phases, when the labelled water parcels were released at: (a) high tide; (b) maximum ebb tide; (c) low tide; (d) maximum flood tide. The colours indicate magnitude (*$cm \cdot s^{-1}$*), and arrows indicate direction.*

Figure 4. *Tidally averaged LRV for different sigma layers in the JZB tide-wind-density system. The Lagrangian residual velocities were deployed at the initial positions of the labelled water parcels. Colours indicate magnitude (*$cm \cdot s^{-1}$*), and arrows indicate direction.*

Figure 5. *Wind-driven, depth-averaged full LRV in the tide-wind-density system at different initial tidal phases when the labelled water parcels were released at (a) high tide; (b) maximum ebb tide; (c) low tide; (d) maximum flood tide.*

Colours indicate magnitude ($cm\cdot s^{-1}$), and arrows indicate direction. Positive values indicate that the wind effect has the same direction as the tide-wind-density driven full LRV, and vice versa.

Figure 6. *Wind-driven, tidally averaged full LRV for different sigma layers in the tide-wind-density system. Full LRV were deployed at the initial positions of the labelled water parcels. Colours indicate magnitude ($cm\cdot s^{-1}$), and arrows indicate direction. Positive values indicate that the wind effect has the same direction as the tide-wind-density driven full LRV, and vice versa.*

Figure 7. *Wind-driven, tidally depth-averaged Lagrangian residual transport velocity in the tide-wind-density system. The Lagrangian residual transport velocities started at the initial positions of the labelled water parcels. Colours indicate magnitude ($cm\cdot s^{-1}$) and arrows indicate direction. Positive values indicate that the wind effect has the same direction as the tide-wind-density driven full LRV, and vice versa.*

Figure 8. *Density-driven, depth-averaged full LRV in the tide-wind-density system when the labelled water parcels were released at different initial tidal phases: (a) high tide; (b) maximum ebb tide; (c) low tide; (d) maximum flood tide. Colours indicate magnitude ($cm\cdot s^{-1}$), and arrows indicate direction. Positive values indicate that the density effect has the same direction as the tide-wind-density driven full LRV, and vice versa.*

Figure 9. *Density-driven, tidally averaged full LRV on different sigma layers in the tide-wind-density system. Full LRV were deployed at the initial positions of the labelled water parcels. Colours indicate magnitude ($cm\cdot s^{-1}$), and arrows indicate direction. Positive values mean that the density effect has the same direction as the tide-wind-density driven full LRV, and vice versa.*

Figure 10. *Density-driven, tidally depth-averaged Lagrangian residual transport velocity in the tide–wind–density system. Lagrangian residual transport velocities were deployed at the initial positions of the labelled water parcels. Colours indicate magnitude ($cm\cdot s^{-1}$), and arrows indicate direction. Positive values mean that the density effect has the same direction as the tide-wind-density driven full LRV, and vice versa.*

Figure 11. *The wind- (left 1) and density- (right 2) driven, depth-averaged ERV in the tide-wind-density system at: (a) high tide; (b) low tide. The other two tidal phases have been omitted, as their ERVs were identical to that for high tide. Colours indicate magnitude ($cm\cdot s^{-1}$), and arrows indicate direction. Positive values mean that the density effect has the same direction as the tide-wind-density driven ERV and vice versa.*

Figure 12. *(a) Semi-analytical solutions for wind-driven flow (as depicted by Winant [2004] under homogeneous conditions, the cross-sectional mean depth (5 m) segregated downwind and upwind flows); (b) wind-driven, full LRV in the tide-wind-density system. The section is that indicated by the dashed line between Huangdao and Hongdao in Figure 1. Negative values denote areas of upwind flow (unit: $cm \cdot s^{-1}$).*

Figure 13. *(a) Semi-analytical solution for density-driven flows (as depicted by Valle-Levinson [2008]); (b) density-driven, full LRV in the tide-wind-density system. The section is that indicated by the dashed line between Huangdao and Hongdao in Figure 1. Negative areas denote upwind flows (unit: $cm \cdot s^{-1}$).*

Figure 14. *Momentum balance across the section for wind-driven full LRV in the JZB tide-wind-density system, at: 1) high tide; 2) low tide. The section is that depicted by the dashed line between Huangdao and Hongdao in Figure 1. Momentum terms integrated along particle trajectories: (a) Tidally averaged, nonlinear advection; (b) viscosity; (c) barotropic pressure gradient; (d) Coriolis forces; (e) baroclinic pressure gradient. Unit: $m^2 \cdot s^{-2}$.*

Figure 15. *Distribution of momentum terms for wind-driven full LRV at 1) high tide and 2) low tide, perpendicular to the section: (a) depth-integrated nonlinear advection; (b) viscosity; (c) barotropic pressure gradient; (d) Coriolis forces; (e) bottom stress; (f) baroclinic pressure gradient; (g) surface wind stress. The section is that depicted by the dashed line between Huangdao and Hongdao in Figure 1. Unit: $m^2 \cdot s^{-2}$, and wind is in the SE direction.*

Figure 16. *Momentum balance in the JZB tide-wind-density system across the section, for density-driven full LRV, at 1) high tide, and 2) low tide, illustrating momentum terms integrated along particle trajectories: (a) tidally averaged, non-linear advection; (b) viscosity; (c) barotropic pressure gradient; (d) Coriolis forces; (e) baroclinic pressure gradient. Unit: $m^2 \cdot s^{-2}$. The section is that depicted by the dashed line between Huangdao and Hongdao in Figure 1.*

Figure 17. *Distribution of momentum terms for density-driven full LRV at 1) high tide, and 2) low tide, perpendicular to the section: (a) depth-integrated nonlinear advection; (b) viscosity; (c) barotropic pressure gradient; (d) Coriolis forces; (e) bottom stress; (f) baroclinic pressure gradient. The section is that depicted by the dashed line between Huangdao and Hongdao in Figure 1. Unit: $m^2 \cdot s^{-2}$.*

Table 1. Numerical experiments used to investigate the effects of wind and density on residual velocity

Table 2. Observed/modelled tidal ellipse parameters for surface semidiurnal tides at the stations in Fig. 1. The tidal ellipse parameters include the semi-major (SEMA, $m \cdot s^{-1}$) and semi-minor (SEMI, $m \cdot s^{-1}$) axes, inclination (Inc, º) and phase (Pha, º). The mean absolute value differences and root mean squares (rms) for the observed and modelled tidal ellipse parameters were also calculated.

Table 3. Observed / modelled Potential Temperature (PT) (℃) and Salinity (Sal) (g / kg) in surface (sur) and bottom (bot) layers, at high (H) and low (L) tides, at the stations in Fig. 1. The mean absolute value differences and rms for the observed and modelled tidal ellipse parameters were also calculated.

Figure 1.

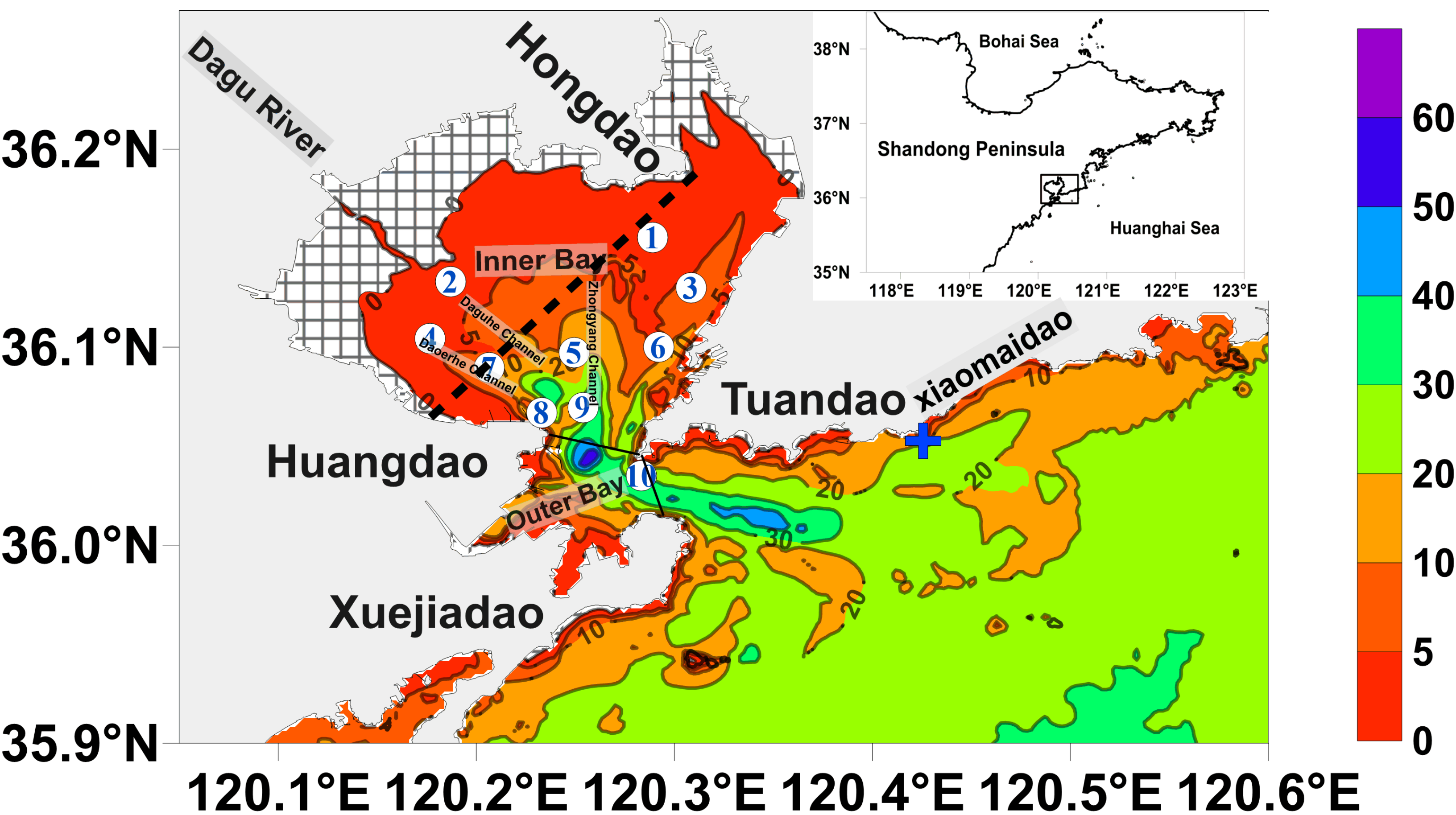

Dagu River
Hongdao
Inner Bay
Daguhe Channel
Daoerhe Channel
Zhongyang Channel
Tuandao
xiaomaidao
Huangdao
Outer Bay
Xuejiadao
Bohai Sea
Shandong Peninsula
Huanghai Sea
38°N
37°N
36°N
35°N
118°E
119°E
120°E
121°E
122°E
123°E
36.2°N
36.1°N
36.0°N
35.9°N
120.1°E
120.2°E
120.3°E
120.4°E
120.5°E
120.6°E
60
50
40
30
20
10
5
0

Figure 2.

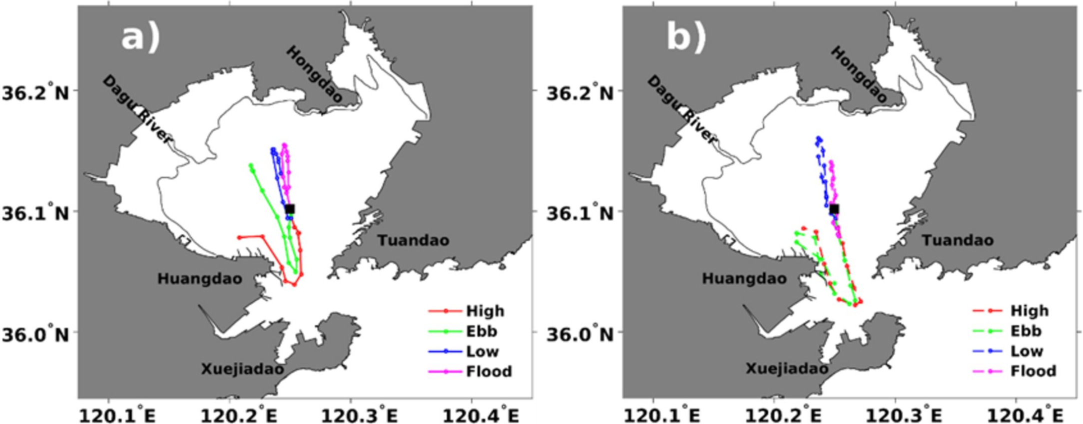

a)
Hongdao
Dagu River
Tuandao
Huangdao
Xuejiadao
High
Ebb
Low
Flood
36.2°N
36.1°N
36.0°N
120.1°E
120.2°E
120.3°E
120.4°E
b)
Hongdao
Dagu River
Tuandao
Huangdao
Xuejiadao
High
Ebb
Low
Flood
36.2°N
36.1°N
36.0°N
120.1°E
120.2°E
120.3°E
120.4°E

Figure 3.

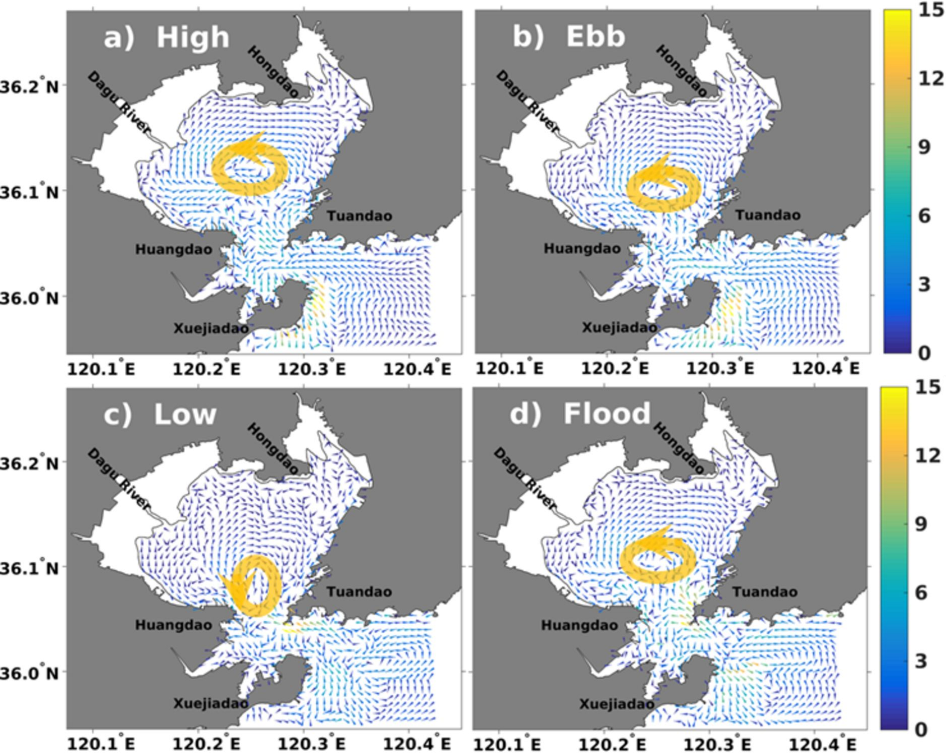

a) High
b) Ebb
c) Low
d) Flood
Dagu River
Hongdao
Tuandao
Huangdao
Xuejiadao
36.2°N
36.1°N
36.0°N
120.1°E
120.2°E
120.3°E
120.4°E
0
3
6
9
12
15

Figure 4.

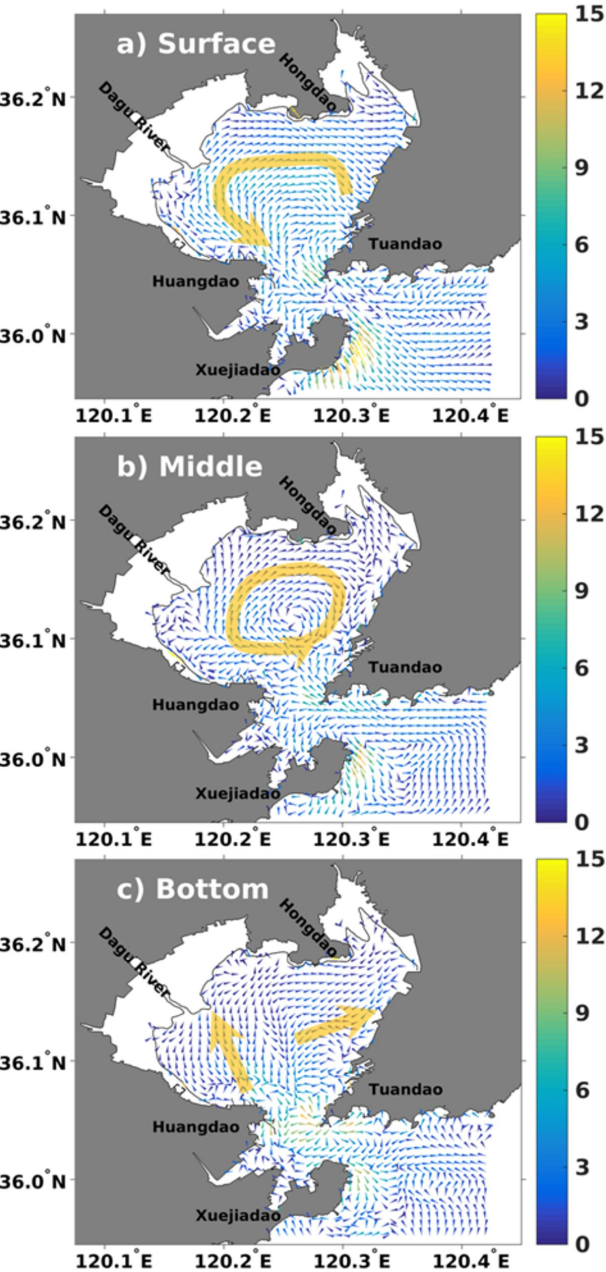
a) Surface
b) Middle
c) Bottom
Hongdao
Dagu River
Tuandao
Huangdao
Xuejiadao
36.2°N
36.1°N
36.0°N
120.1°E
120.2°E
120.3°E
120.4°E
0
3
6
9
12
15

Figure 5.

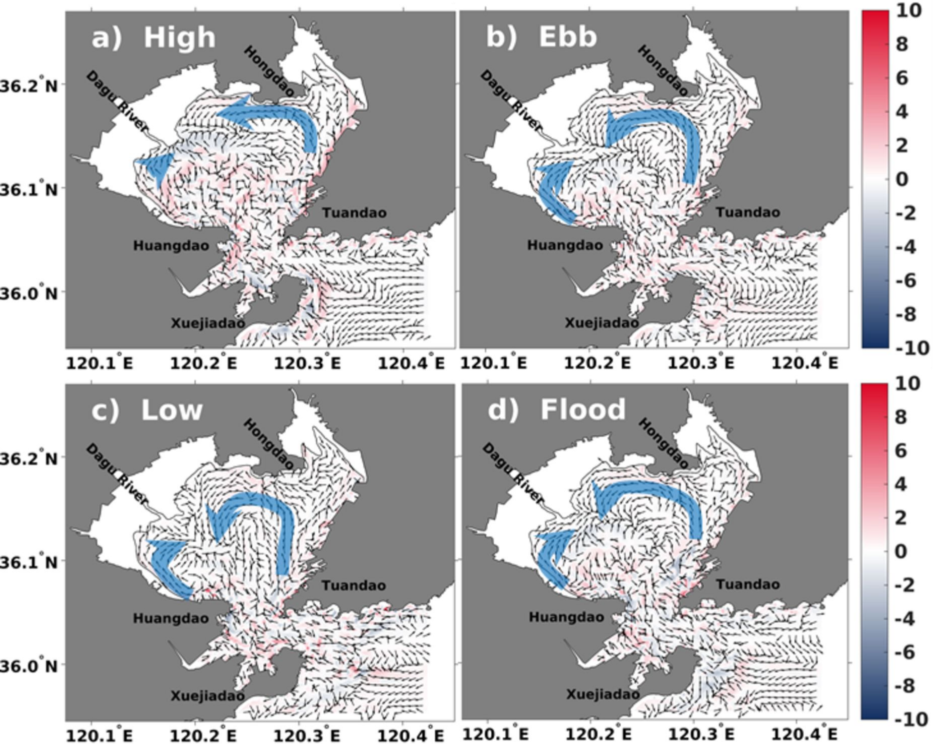
a) High
b) Ebb
c) Low
d) Flood
Hongdao
Dagu River
Tuandao
Huangdao
Xuejiadao
36.2°N
36.1°N
36.0°N
120.1°E
120.2°E
120.3°E
120.4°E
10
8
6
4
2
0
-2
-4
-6
-8
-10

Figure 6.

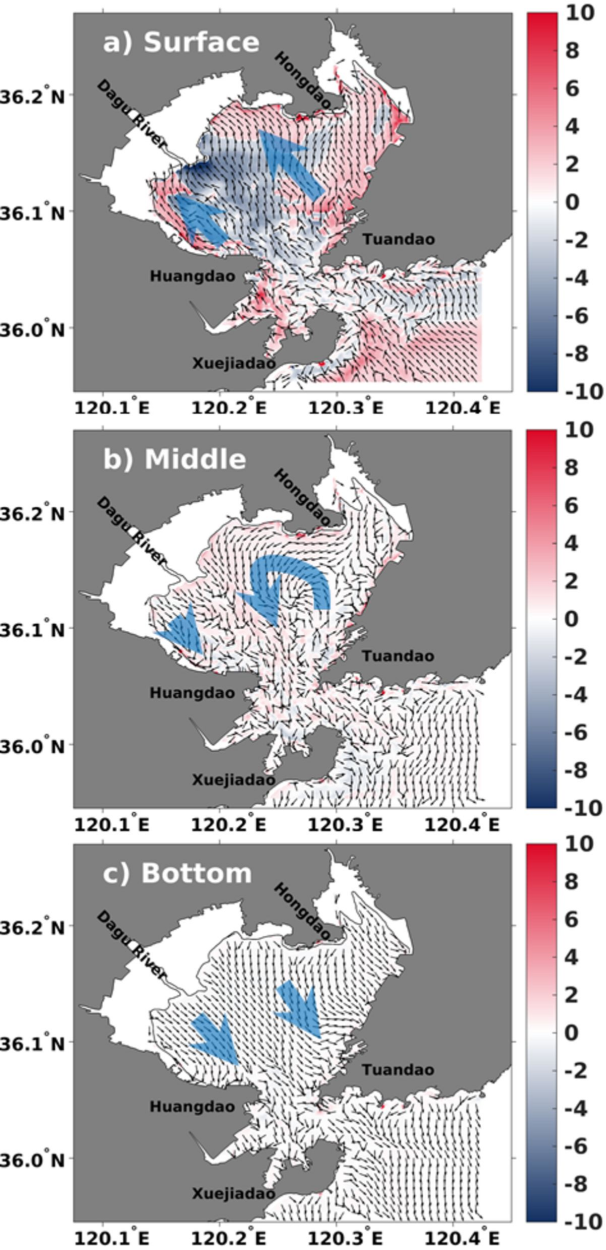
a) Surface
b) Middle
c) Bottom
Hongdao
Dagu River
Tuandao
Huangdao
Xuejiadao
36.2°N
36.1°N
36.0°N
120.1°E
120.2°E
120.3°E
120.4°E
10
8
6
4
2
0
-2
-4
-6
-8
-10

Figure 7.

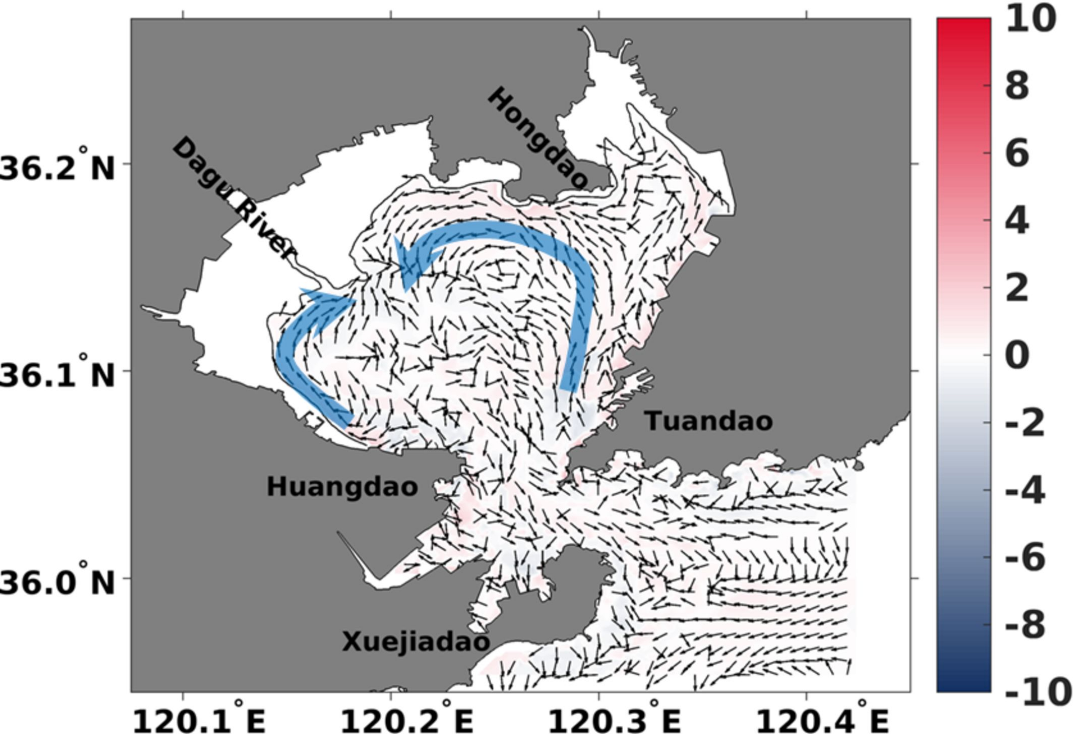

Hongdao
Dagu River
Tuandao
Huangdao
Xuejiadao
36.2°N
36.1°N
36.0°N
120.1°E
120.2°E
120.3°E
120.4°E
10
8
6
4
2
0
-2
-4
-6
-8
-10

Figure 8.

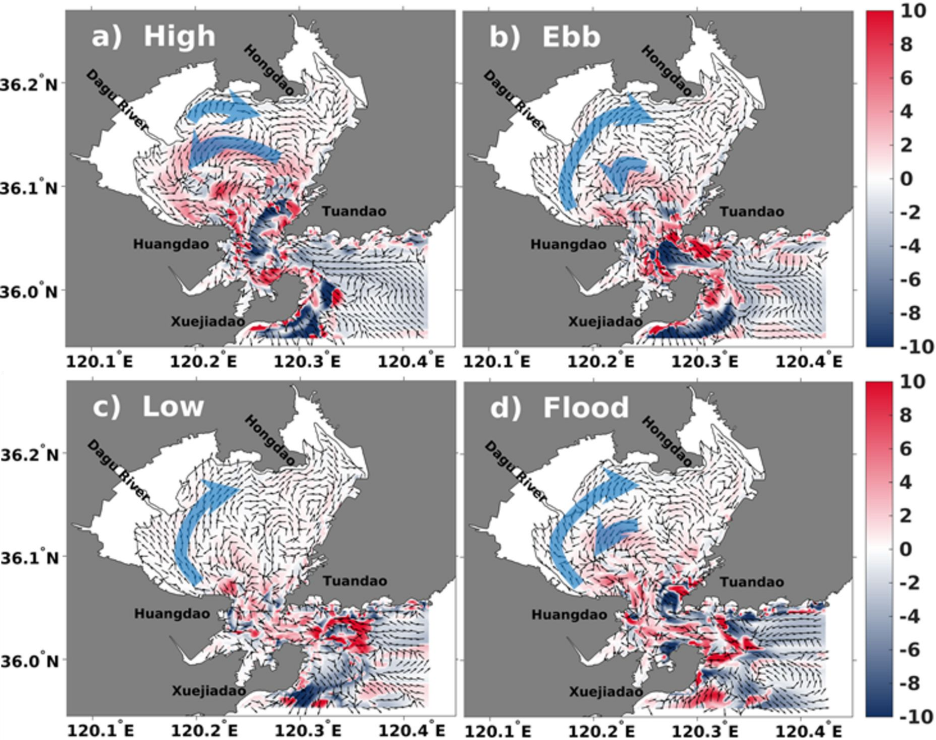

a) High
b) Ebb
c) Low
d) Flood
Hongdao
Dagu River
Tuandao
Huangdao
Xuejiadao
36.2°N
36.1°N
36.0°N
120.1°E
120.2°E
120.3°E
120.4°E
10
8
6
4
2
0
-2
-4
-6
-8
-10

Figure 9.

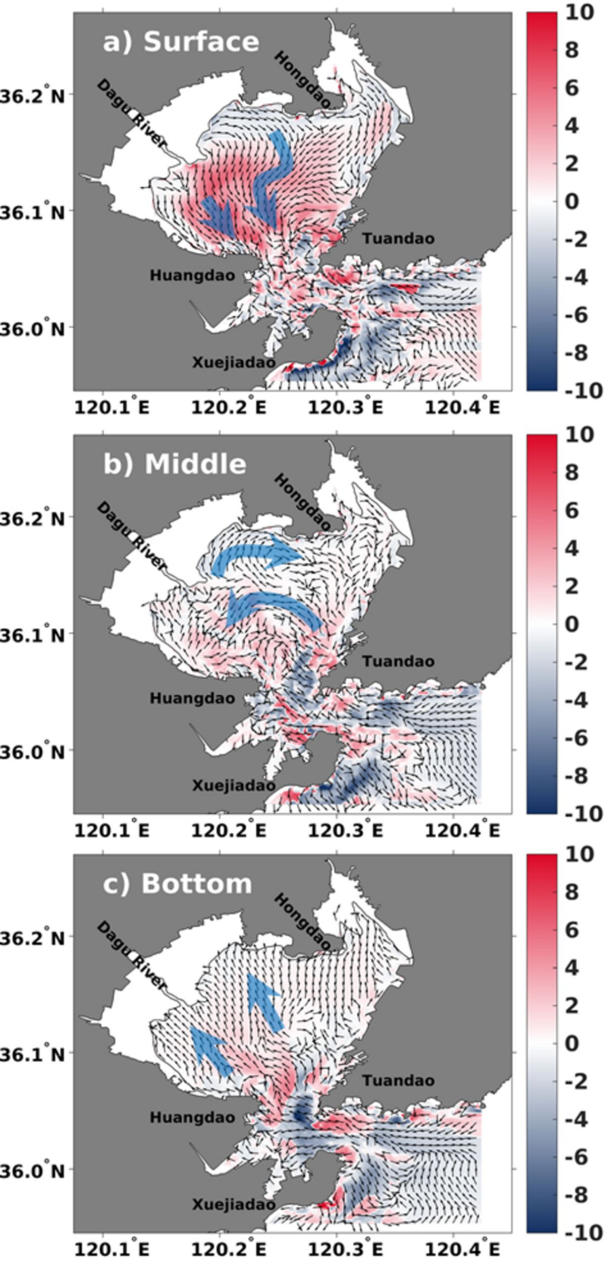

a) Surface
b) Middle
c) Bottom
Hongdao
Dagu River
Tuandao
Huangdao
Xuejiadao
36.2°N
36.1°N
36.0°N
120.1°E
120.2°E
120.3°E
120.4°E
10
8
6
4
2
0
-2
-4
-6
-8
-10

Figure 10.

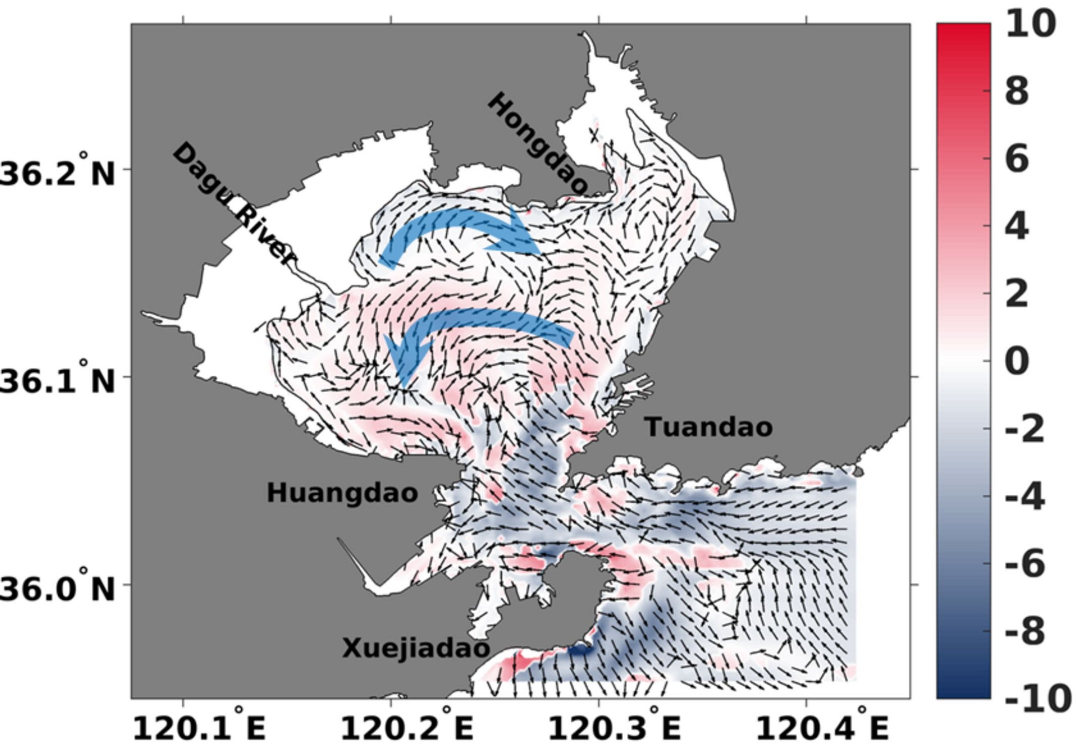

Hongdao
Dagu River
Tuandao
Huangdao
Xuejiadao
36.2°N
36.1°N
36.0°N
120.1°E
120.2°E
120.3°E
120.4°E
10
8
6
4
2
0
-2
-4
-6
-8
-10

Figure 11.

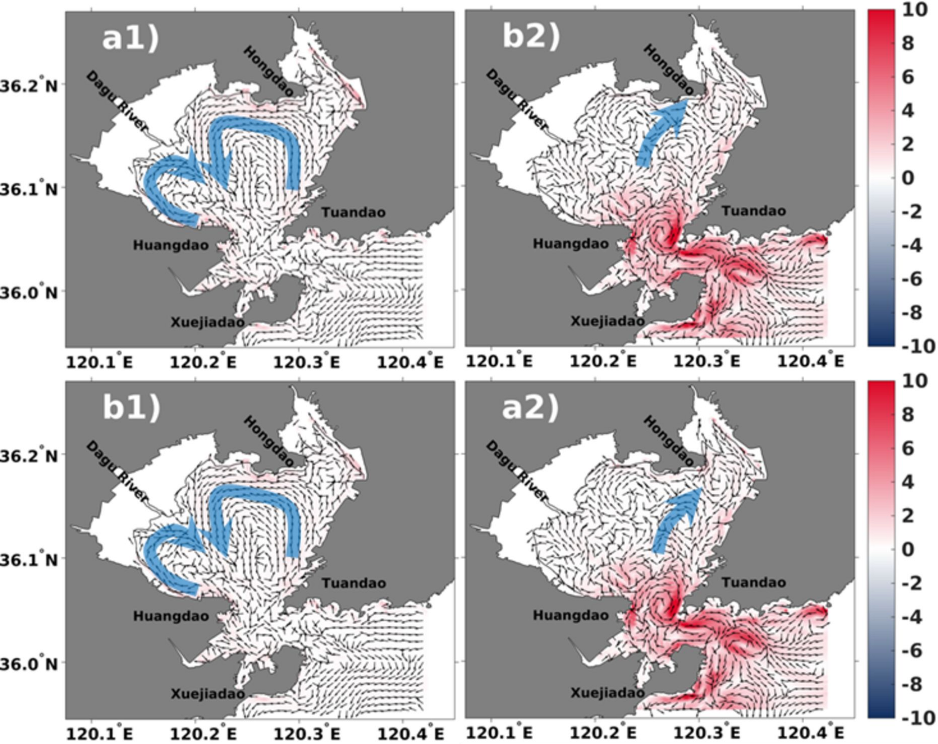
a1)
b2)
b1)
a2)
Dagu River
Hongdao
Tuandao
Huangdao
Xuejiadao
36.2°N
36.1°N
36.0°N
120.1°E
120.2°E
120.3°E
120.4°E
10
8
6
4
2
0
-2
-4
-6
-8
-10

Figure 12.

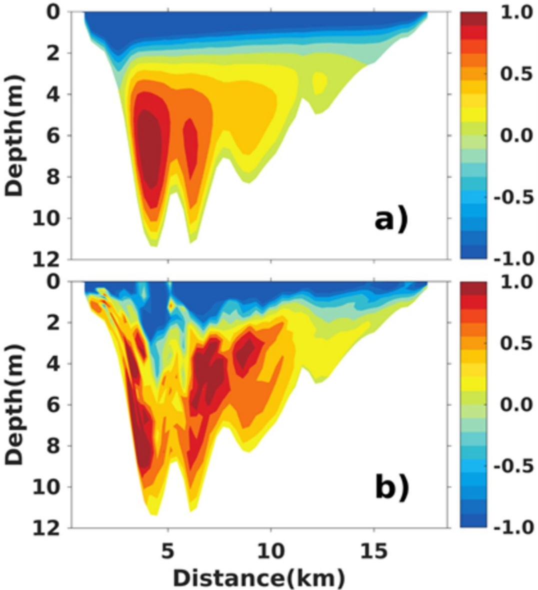

0
2
4
6
8
10
12
Depth(m)
a)
1.0
0.5
0.0
-0.5
-1.0
0
2
4
6
8
10
12
Depth(m)
b)
1.0
0.5
0.0
-0.5
-1.0
5
10
15
Distance(km)

Figure 13.

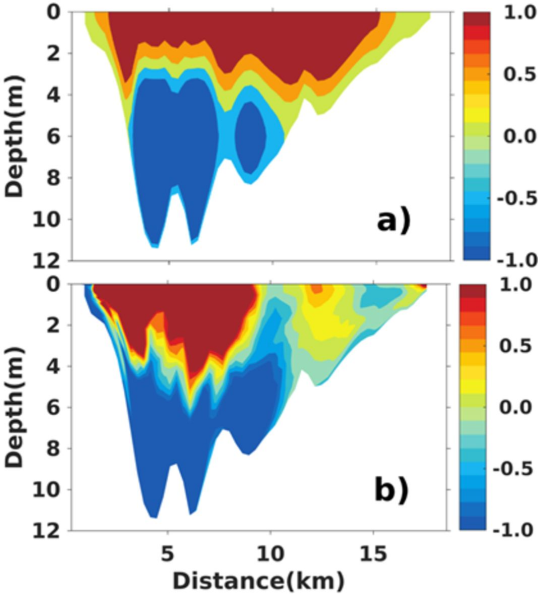

a)
b)
Depth(m)
Depth(m)
0
2
4
6
8
10
12
5
10
15
Distance(km)
1.0
0.5
0.0
-0.5
-1.0

Figure 14.

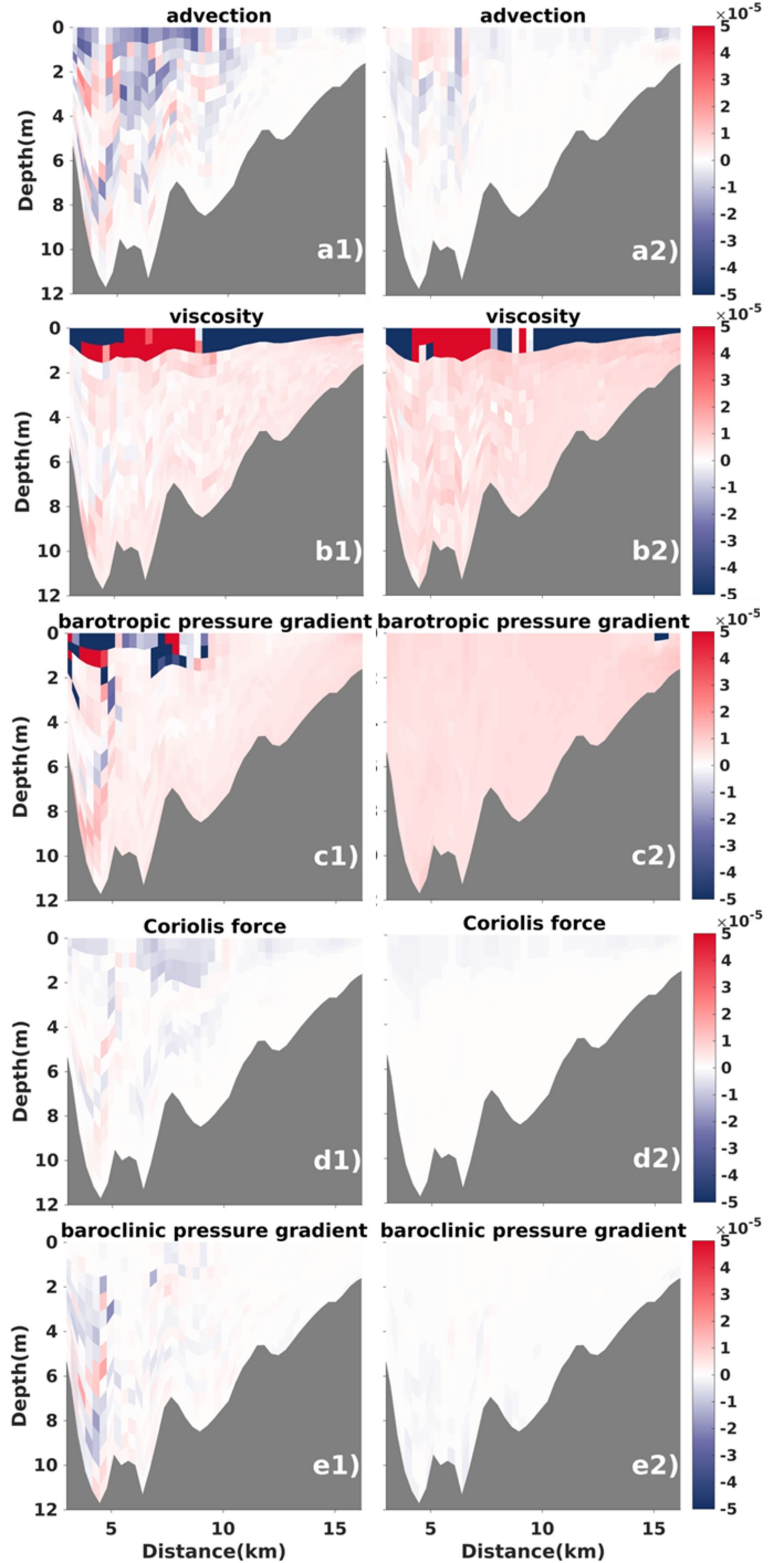
advection
advection
viscosity
viscosity
barotropic pressure gradient
barotropic pressure gradient
Coriolis force
Coriolis force
baroclinic pressure gradient
baroclinic pressure gradient
Depth(m)
Distance(km)
a1)
a2)
b1)
b2)
c1)
c2)
d1)
d2)
e1)
e2)
×10^-5

Figure 15.

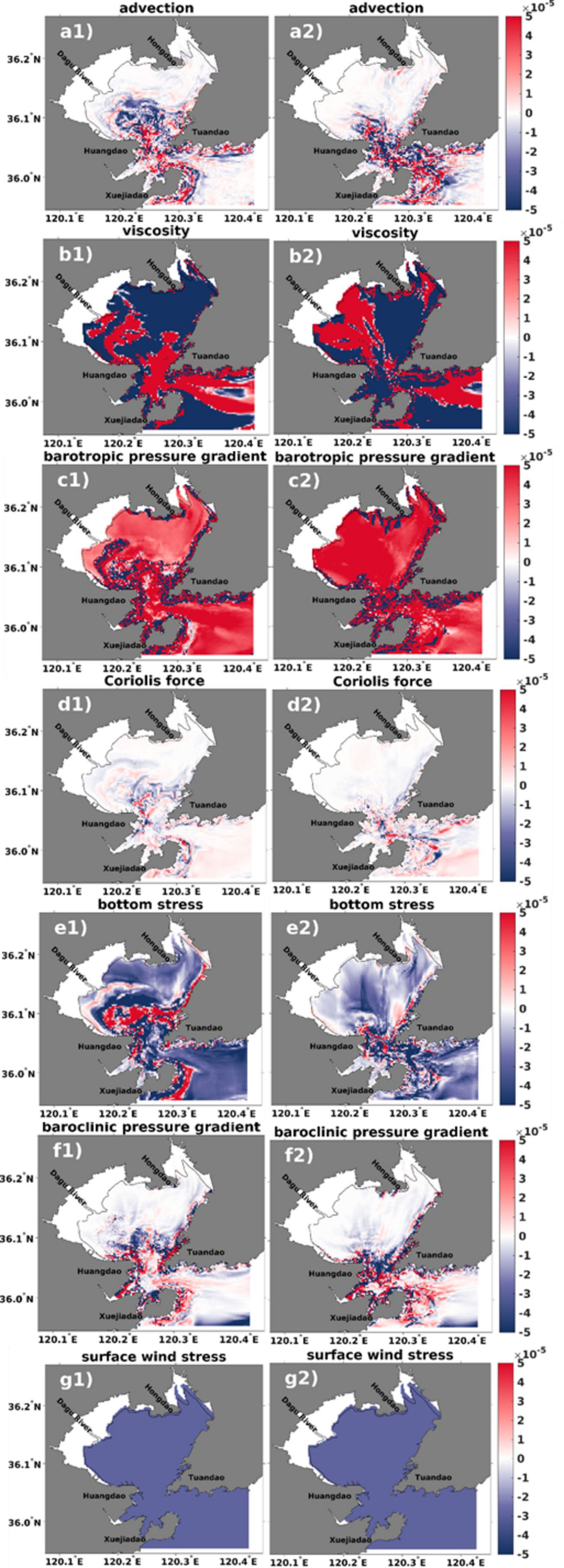
advection
a1)
a2)
viscosity
b1)
b2)
barotropic pressure gradient
c1)
c2)
Coriolis force
d1)
d2)
bottom stress
e1)
e2)
baroclinic pressure gradient
f1)
f2)
surface wind stress
g1)
g2)
Hongdao
Dagu River
Tuandao
Huangdao
Xuejiadao
36.2°N
36.1°N
36.0°N
120.1°E
120.2°E
120.3°E
120.4°E
×10^-5
5
4
3
2
1
0
-1
-2
-3
-4
-5

Figure 16.

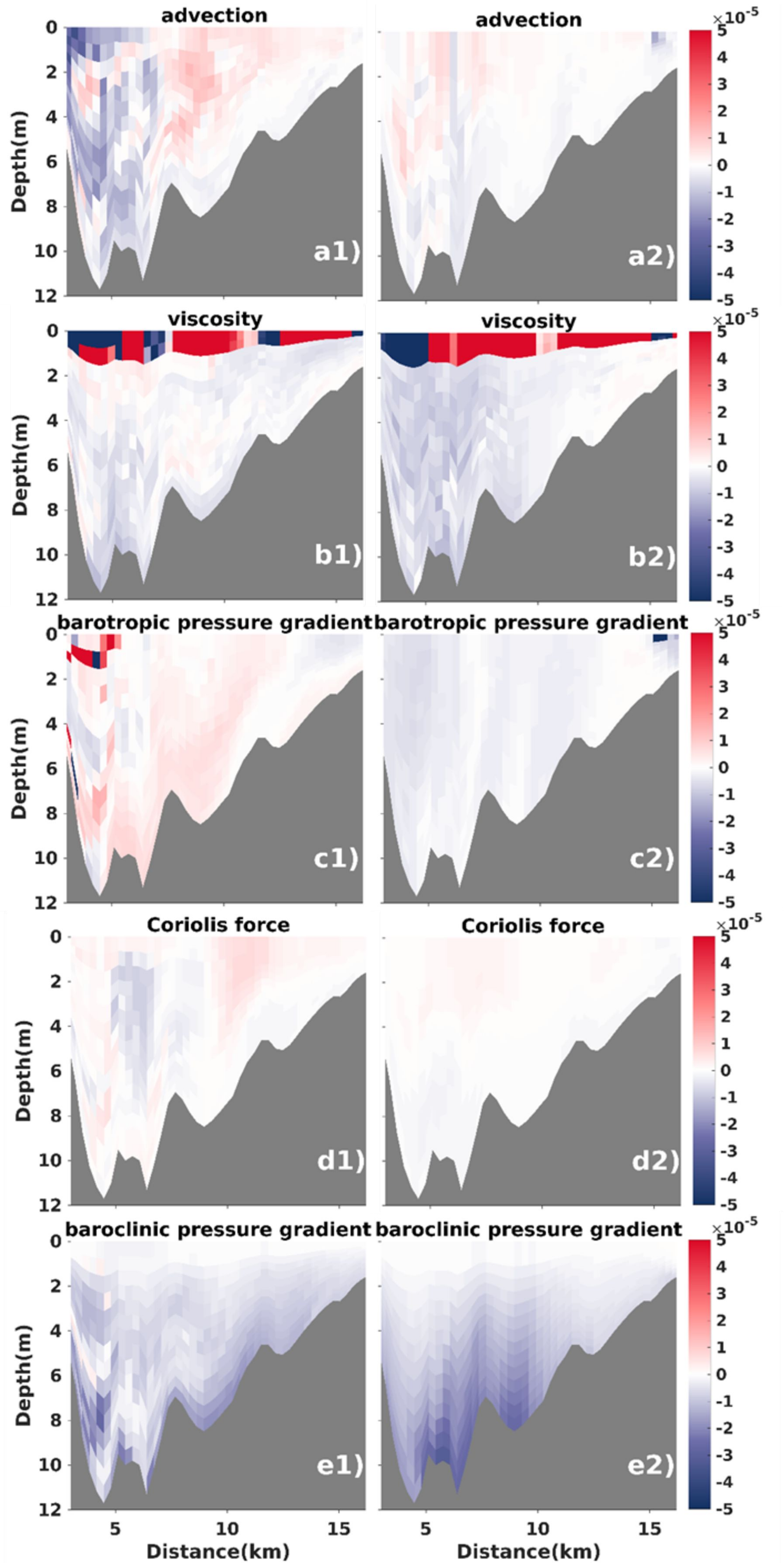

advection
advection
viscosity
viscosity
barotropic pressure gradient
barotropic pressure gradient
Coriolis force
Coriolis force
baroclinic pressure gradient
baroclinic pressure gradient
a1)
a2)
b1)
b2)
c1)
c2)
d1)
d2)
e1)
e2)
Depth(m)
Distance(km)
$\times 10^{-5}$

Figure 17.

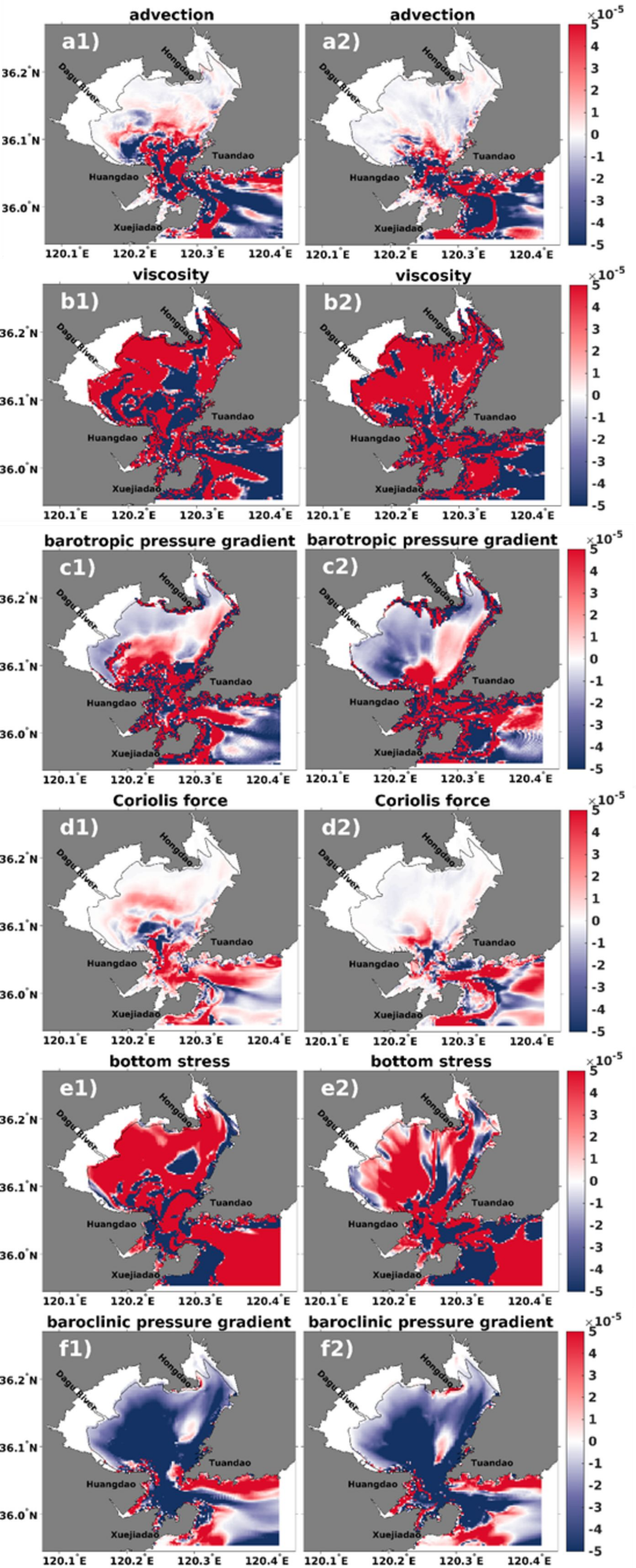
advection
a1)
a2)
viscosity
b1)
b2)
barotropic pressure gradient
c1)
c2)
Coriolis force
d1)
d2)
bottom stress
e1)
e2)
baroclinic pressure gradient
f1)
f2)
Hongdao
Dagu River
Tuandao
Huangdao
Xuejiadao
36.2°N
36.1°N
36.0°N
120.1°E
120.2°E
120.3°E
120.4°E
×10^-5
5
4
3
2
1
0
-1
-2
-3
-4
-5